Toward Crop Maturity Assessment via UAS-Based Imaging Spectroscopy—A Snap Bean Pod Size Classification Field Study

Amirhossein Hassanzadeh, *Student Member, IEEE*, Fei Zhang, *Student Member, IEEE*, Sean P. Murphy, *Member, IEEE*, Sarah J. Pethybridge, *Member, IEEE*, and Jan van Aardt, *Member, IEEE*

***Abstract*— Timely assessment of crop maturity contributes to optimized harvesting schedules while limiting food loss/waste at the farm level. Maturity assessments are typically performed via costly and time-consuming *in situ* methods. This study aimed to evaluate pod size crop maturity using imaging spectroscopy via unmanned aerial systems (UASs), as well as identifying discriminating wavelengths, using snap bean as a proxy crop. The research utilized a UAS-mounted hyperspectral imager in the visible-to-near-infrared region. Two years' worth of data were collected at two different geographical locations for six different snap bean cultivars. Our approach consisted of calibration to reflectance, vegetation detection, noise reduction, creating classification bins, and feature selection. We used our previously published feature selection library, Jostar, and utilized ant colony optimization and simulated annealing to detect five spectral features and Plus-L Minus-R to identify one to ten features. We utilized decision trees and random forest classifiers for the classification task. Our findings show that, given the proper wavelengths, accurate pod maturity assessment is feasible for large-sieve cultivars (F1 score = 0.79–0.91), separating sieve sizes between ready-to-harvest and not ready-to-harvest pods. These spectral features were in the ∼450, ∼530, ∼660, 700–720, ∼740, and ∼760 nm regions. This bodes well for the potential extension of results to an operational, multispectral sensor, tuned with the identified bands, thereby negating the need for a costly hyperspectral system. However, this proposition mandates further investigation, including data acquisition from geographical locations with variable climates, and quantifying noise for the hyperspectral imager to compare results with noisier datasets.**

***Index Terms*— Classification, feature selection, hyperspectral imaging, machine learning, maturity assessment, pod size, precision agriculture, snap bean, unmanned aerial system (UAS).**

Manuscript received September 25, 2021; revised October 29, 2021; accepted December 2, 2021. Date of publication December 10, 2021; date of current version March 1, 2022. This work was supported by the National Science Foundation Partnerships for Innovation (PFI) Program under Award 1827551. *(Corresponding author: Amirhossein Hassanzadeh.)*

Amirhossein Hassanzadeh, Fei Zhang, and Jan van Aardt are with the Chester F. Carlson Center for Imaging Science, Rochester Institute of Technology, Rochester, NY 14623 USA (e-mail: ah7557@rit.edu).

Sean P. Murphy and Sarah J. Pethybridge are with the Plant Pathology and Plant-Microbe Biology Section, School of Integrative Plant Science, Cornell AgriTech at The New York State Agricultural Experiment Station, Cornell University, Ithaca, NY 14850 USA.

Digital Object Identifier 10.1109/TGRS.2021.3134564

I. Introduction

UP TO 30% of food waste occurs at the farm level when the harvested produce does not match the required quality, quantity, and dimensions [6]. The assumption of uniform distribution of growth across a field furthermore is far from reality, resulting in overmature and undermature harvested produces. It, therefore, stands to reason that, if farmers and growers knew when and where to harvest, crop production in terms of both quality and quantity could be optimized. However, most current protocols for crop maturity assessment require time- and resource-intensive *in situ* approaches, thus indicating a need for a rapid, remote, nondestructive approach.

Remote sensing (RS) can satisfy these requirements by collecting data of a target area via unmanned aerial systems (UASs) for a range of different sensing modalities. These modalities vary from light detection and ranging (LiDAR), color (RGB), and synthetic aperture radar (SAR) to spectral systems (multispectral and hyperspectral), with applications spanning climate monitoring, forest inventory management, and crop assessment, among others [23], [41], [44], [55], [65], [67], [73]. In terms of spectral systems, hyperspectral imagery (HSI) collects pixel-level spectral information within a specific domain of the electromagnetic energy, spanning to hundreds of contiguous bands (or wavelengths) [39]. Hyperspectral sensors can play a key role in studying crops since the captured spectral response, in theory, is representative of a crop's biochemical composition and intercellular and molecular structure, especially in the visible-to-near-infrared (VNIR) spectral region [18], [56], [68]. In other words, the change in biochemical and structural features can be observed in the crop spectral signature. This physiological link between crop status and the spectral response has motivated researchers to also assess crop maturity through the lens of HSI. Studies focused on crop maturity fall into two categories: 1) maturity assessment based on biophysical indicator estimation, such as dry matter (DM), moisture content (MC), firmness, total soluble solids (TSSs), and total acidity (TA) [4], [5], [20], [33], [40], [45], [49], [51] and 2) more general crop maturity stage classification [17], [22], [42], [75]. The former approach requires laboratory measurements as ground-truth data (more labor-intensive to obtain), while ground-truth data collection

for the latter approach is relatively straightforward and less complex (i.e., class labels). However, an often overlooked aspect of HSI data is the need for robust preprocessing, most notably in terms of noise reduction, given the narrow bandwidths [10].

Hyperspectral data are potentially noisy and consist of highly correlated spectral features that need to be subselected to fit the objective. This mandates preprocessing of HSI prior to input to predictive models [47], [53]. The noise in hyperspectral data also could be due to inherent instrument noise, such as quantization noise and photon noise [21], [32], [52]. There have been numerous studies that shed light on hyperspectral denoising using wavelet transforms [11], [28], [37], total variation (TV) models [2], [70], and deep learning models [29], [72]. Among these algorithms, the method proposed by Chen and Qian [11], utilizing the principal component analysis (PCA) and wavelet transforms, has gained considerable attention although it requires manual selection of the number of principal components (PCs) to retain. Second, the collected hyperspectral data are typically highly correlated (especially in adjacent bands [35]), meaning that one variable could be determined by another with a high degree of accuracy. Such correlated features can cause overfitting in machine learning models [25]. Often, the correlation coefficient (R) is used to determine the extent to which two variables are correlated [8]. Third, even after decorrelation, large number of features may not be explanatory in terms of the objective being studied, i.e., this step calls for feature selection methods [36]. Feature selection approaches have proven effective for high-dimensional data and fall into three categories, namely, filter, wrapper, and embedded methods [63]. Filter methods provide a score for each variable and explain how much each variable contributes to the objective function (i.e., reference values), with examples such as mutual information, variance, and RReliefF [7], [54]. Score calculation is computationally cheap, but filter methods are not as accurate as other approaches since they do not take into account the relationship between features. On the other hand, wrapper methods initially rely on a trial-and-error approach while expanding on that via their particular optimization algorithm. Wrapper methods have proven to be more accurate since they take account of the interaction between features even though they are computationally expensive. Examples of wrapper methods include sequential feature selection (SFS [3]), simulated annealing (SA [60]), ant colony optimization (ACO [14]), and genetic algorithm (GA [66]) approaches. Embedded methods, as the name suggests, provide a calculated score embedded in the training process [43]. Although these methods are faster when compared to wrapper methods, they may not be as accurate. The abovementioned preprocessing techniques have appeared in the literature and were employed by various studies for the assessment of crop maturity using hyperspectral data.

A large body of literature consists of maturity estimation based on biophysical indicators, while there is a general lack of research regarding crop maturity classification. Yang *et al.* [69] conducted blueberry growth stage classification (young, intermediate, mature stage) using ground-based HSI in the VNIR region. The study employed three different classifiers, namely, the support vector machine (SVM), the K-nearest neighbor (KNN), and AdaBoost, along with Kullback–Leibler divergence (KL divergence), hierarchical dimensionality reduction, and non-Gaussian measures as band selection methods. Their findings show accuracies above 88% for the classification of blueberry growth stages. Recently, Singh *et al.* [57] used UAS-based HSI (VNIR) for canola pod maturity estimation, at five different pod sieve sizes, for five canola genotypes. Their results show that their introduced vegetation index (VI) (canola pod maturity index [CPMI]) can estimate canola pod moisture with a coefficient of determination (R^2) as high as 0.98, with only three selected bands. Tao *et al.* [59] estimated above-ground biomass (AGB) and leaf area index (LAI) of winter wheat at four different growth stages using HSI (VNIR) and concluded that the plant biochemical index (PBI) and linear combination index (LCI) had the highest correlation coefficient with the mentioned VIs. Their findings showed that the flowering stage had the highest accuracies, with $R^2 > 0.65$ and normalized root-mean-square error (nRMSE) as low as 14%. Zou *et al.* [75], in turn, used a laboratory-based HSI (VNIR) system to assess peanut maturity for two classes (mature versus immature) over two years of data via a fully constrained least squares unmixing approach. Their findings show accuracies above 83% for the testing set.

The majority of crop maturity assessment studies are limited to one crop cultivar, restricted to one geographical location for data collection, and a single temporal evaluation of the crop. Moreover, little research has been done regarding the maturity classification of crops using hyperspectral imaging. With a market value of approximately $300 million in 2019, snap bean *(Phaseolus vulgaris)* is considered one of the largest crops in the United States [1]. Snap bean's important role in our everyday diet [46], along with its short growth period (55–65 days) makes this crop an ideal proxy crop for growth maturity assessment. However, the snap bean has not received much attention in the literature. Here, we focus on snap bean (as a proxy crop) over six different cultivars toward addressing the hypothesis that snap bean maturity (pod size) assessment can be addressed with HSI, given that maturity is reflected by canopy-level spectral features. The objectives of this study were to identify discriminating spectral features via feature selection methods, corresponding best with the classification of maturity stages of snap bean, and evaluate the feasibility of using machine learning algorithms for classification between different crop maturity stages, in terms of snap bean pod size.

II. Materials and Methods

A. Study Area

This study was conducted at two geographical locations, Geneva, NY, USA (42°49'53.0" N, 77°00'48.2" W), for summer 2019, and Seneca, NY, USA (42°51'59.2" N, 77°01'45.8" W), for summer 2020. The 2019 dataset consisted of 24 plots, and the 2020 dataset contained 18 experimental plots, with each plot being 1.5 m long and 0.75 m wide. Six different cultivars of snap bean, namely, Venture (L1), Huntington (L2), Colter (F1), Cabot (F2), Flavor-sweet (W1), and Denver (W2), were sowed in two experimental fields, for both years,

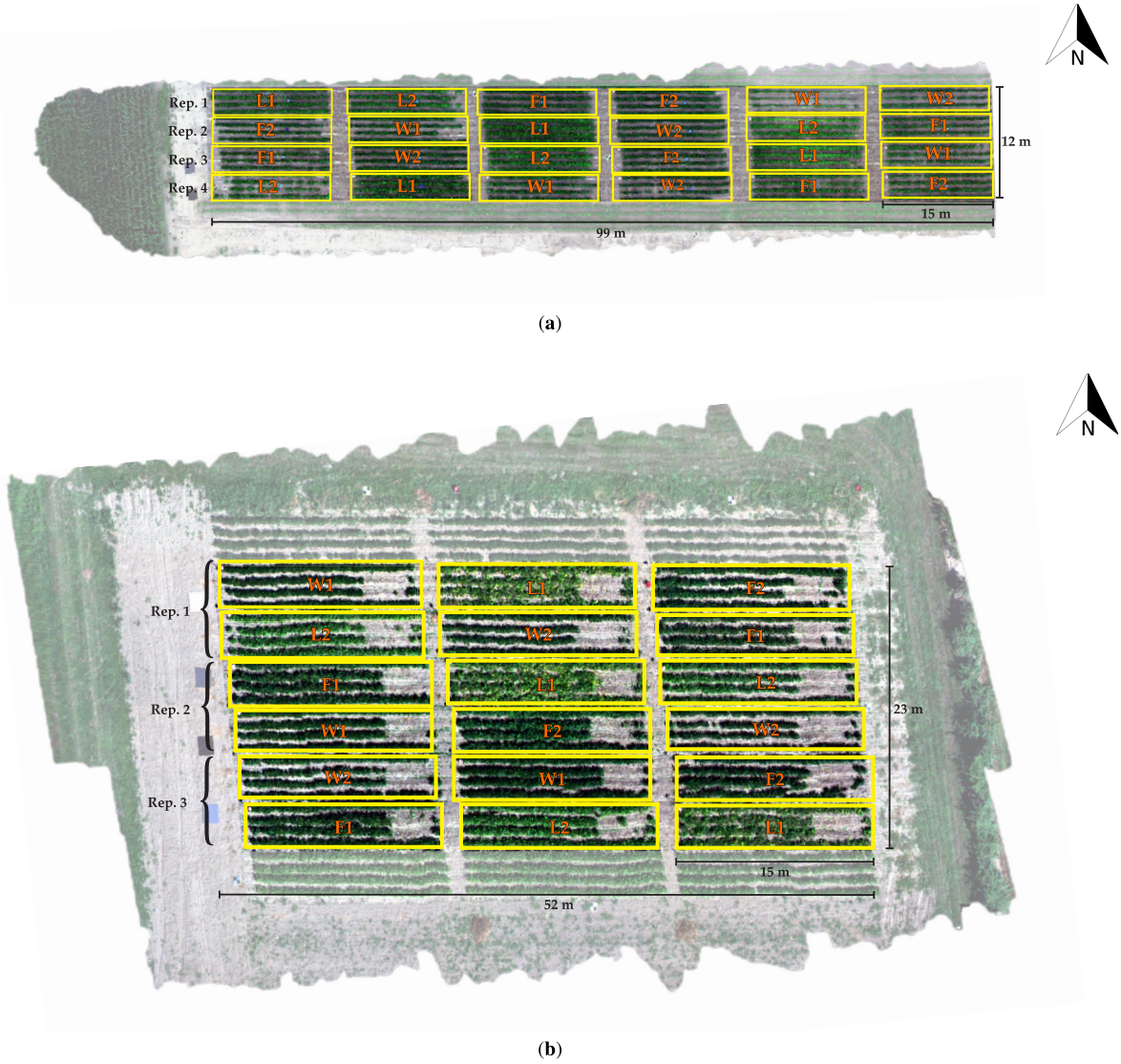

Fig. 1. Plot outlines and corresponding dimensions for (a) 2019 and (b) 2020 datasets. The snap bean cultivars were L1: Venture; L2: Huntington; F1: Colter; F2: Cabot; W1: Flavor-sweet; and W2: Denver.

to ensure integration between different varieties, i.e., two from large-sieve cultivars (L1 and L2), two from four-sieve cultivars (F1 and F2; the largest pod size for this group is sieve size four), and two from whole bean cultivars (W1 and W2). Each cultivar's plot was replicated four times for the 2019 dataset and three times for the 2020 dataset. Fig. 1 shows the RGB representation of the experimental fields and the outline of designated plots. The total trial dimensions were 99×12 m and 52×23 m for 2019 and 2020 datasets, respectively.

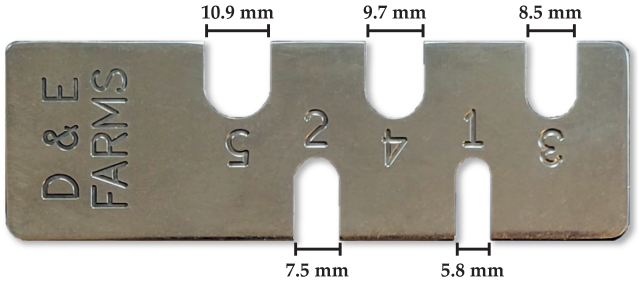

Fig. 2. Sieve gauge used for pod sieve size measurement.

B. Plant Growth Characteristics

For both datasets, seeds were sowed at 20–26 plants/m at an approximate depth of 3.8 cm. At planting, fertilizer with a ratio of 15:5:5 (N:P:K) with a rate of 335 kg/ha was applied. Pod size ground-truth data were collected concurrently with the flights. At each evaluation, a 3 m sample of the plot was selected, and pods from plants were further investigated for sieve size, as a maturity indicator. To classify pods into sieve sizes, pods are slid across cavities of a sieve gauge, as depicted in Fig. 2. Six sieve sizes ($S1$–$S6$) corresponding to the following sizes were determined for the pods: $S1 <$ 5.8 mm; 5.8 mm $< S2 <$ 7.5 mm; 7.5 mm $< S3 <$ 8.5 mm;

TABLE I
INFORMATION ON DATA COLLECTION FOR 2019 AND 2020 DATASETS DURING SNAP BEAN POD FORMATION STAGES

Year	Flight Date	GSD* (cm)	Altitude (m)	Velocity (m/s)	Days After Planting (DAP)
2019	08/12/2019	1.5	24	2.5	46
	08/14/2019	3	48	2.5	48
	08/16/2019	3			50
	08/20/2019	3			54
	08/22/2019	3			56
2020	08/10/2020	3			44
	08/14/2020	3			48
	08/21/2020	3			55
	08/24/2020	3			58
	08/26/2020	3			60

* Ground Sampling Distance

8.5 mm $< S4 <$ 9.7 mm; 9.7 mm $< S5 <$ 10.9 mm; and $S6 >$ 10.9 mm. Total weight per sieve size, for the top two largest sieve sizes identified, was logged for each cultivar using (Model "ES6R," OHAUS Corporation, Parsippany, NJ, USA; 0.002-kg precision). Consequently, the sieve size with the largest weight was assigned to the plot's class.

C. Data Collection

A hyperspectral imager ("Nano Hyperspec" model, Headwall Photonics, Fitchburg, MA, USA) was mounted on a DJI Matrice-600 quadcopter. The hyperspectral imager is a pushbroom sensor with a slit of 640 pixels across and a full-width at half-maximum (FWHM) of 6 nm. Five flights were conducted for both 2019 and 2020 datasets during the crop pod formation stage (i.e., the reproductive stage). Table I shows the flight data collection information, along with days after planting (DAP). The weather condition for all flights was uniformly sunny or uniformly cloudy (i.e., minimal change in illumination conditions).

D. Data Preprocessing and Analysis

Five major steps, as depicted in Fig. 3, were employed for preprocessing and analysis of the collected HSI data. The data preprocessing stage included calibration to reflectance, plot extraction and vegetation detection, noise reduction, and data preparation. The data analysis stage included applying our previously introduced feature selection library (Jostar [24]) to preprocessed data. Each of the mentioned stages will be explored next.

1) Calibration to Reflectance: The empirical line method (ELM [58]) was utilized for calibration to reflectance. Three- and four-point configurations for the ELM approach were conducted for 2019 and 2020 datasets, respectively. This method forces the drone spectra to match those from the field spectra (via a spectroradiometer) by applying a gain and an offset to each band. We utilized a portable spectroradiometer ("HR-1024i" model, Spectra Vista Corporation, Poughkeepsie, NY, USA) for collecting the field spectra. The resulting hyperspectral data cube, in reflectance, was then passed to the next step for plot extraction and vegetation detection.

2) Plot Extraction and Vegetation Detection: Distinguishable pink markers were placed on the northeast end of each plot. Marker positions, along with the captured ground sampling distance (GSD), were used to automatically define regions of interest for the detection of plot boundaries. After extracting plots from the hyperspectral data cube, we chose the spectral angle mapper (SAM [71]) for vegetation detection (formula shown in Fig. 3) since it is relatively insensitive to changes in illumination [34]. SAM calculates the cosine similarity angle between two vectors, namely, a reference and an input vector. The input vector was a spectrum from the hyperspectral data, and the reference vector is generally drawn from a spectral library, imagery samples, or ground data [74]. In this study, we used the average spectrum of our previously published spectral library of more than 1000 samples of snap bean, captured in a greenhouse [22]. A threshold (θ) with a value of 0.3-rad (chosen by trial and error) was used to separate the vegetation from the background. The identified vegetation spectra were then passed to the noise reduction step.

3) Noise Reduction: The noise reduction stage consisted of two steps. First, since the signal-to-noise ratio (SNR) in the detector fall-off regions was lower than in other domains, we removed bands in the 400–450 and 900–1000 nm domains. This, in turn, reduced the number of bands from 272 to 202. We then employed the spectral denoising approach by Chen and Qian [11], as described in Section I. This approach uses PCA and transforms the spectral data to the PC space. Subsequently, a number of crucial PCs are retained, and the rest are passed to the spectral denoising algorithm. In the published work, the authors select the number of retained PCs via visual assessment of the projected data in the PCA spatial space. We aimed to utilize the proposed method only in the spectral domain (1-D) and not the spatial domain. As a result, visual assessment of hundreds of bands would be impossible, and thus, a more automated approach was needed. Two extensively used methods for retaining top-k PCs, namely, the minimum average partial (MAP [62]) and eigenvalue greater than one (Kaiser [31]), and, thus, were utilized and compared in this study. The identified k PCs were retained and (p-k) PCs were then passed to dual-tree wavelet complex transform at five different levels. The threshold method, proposed by Chen and Qian [11], then was applied

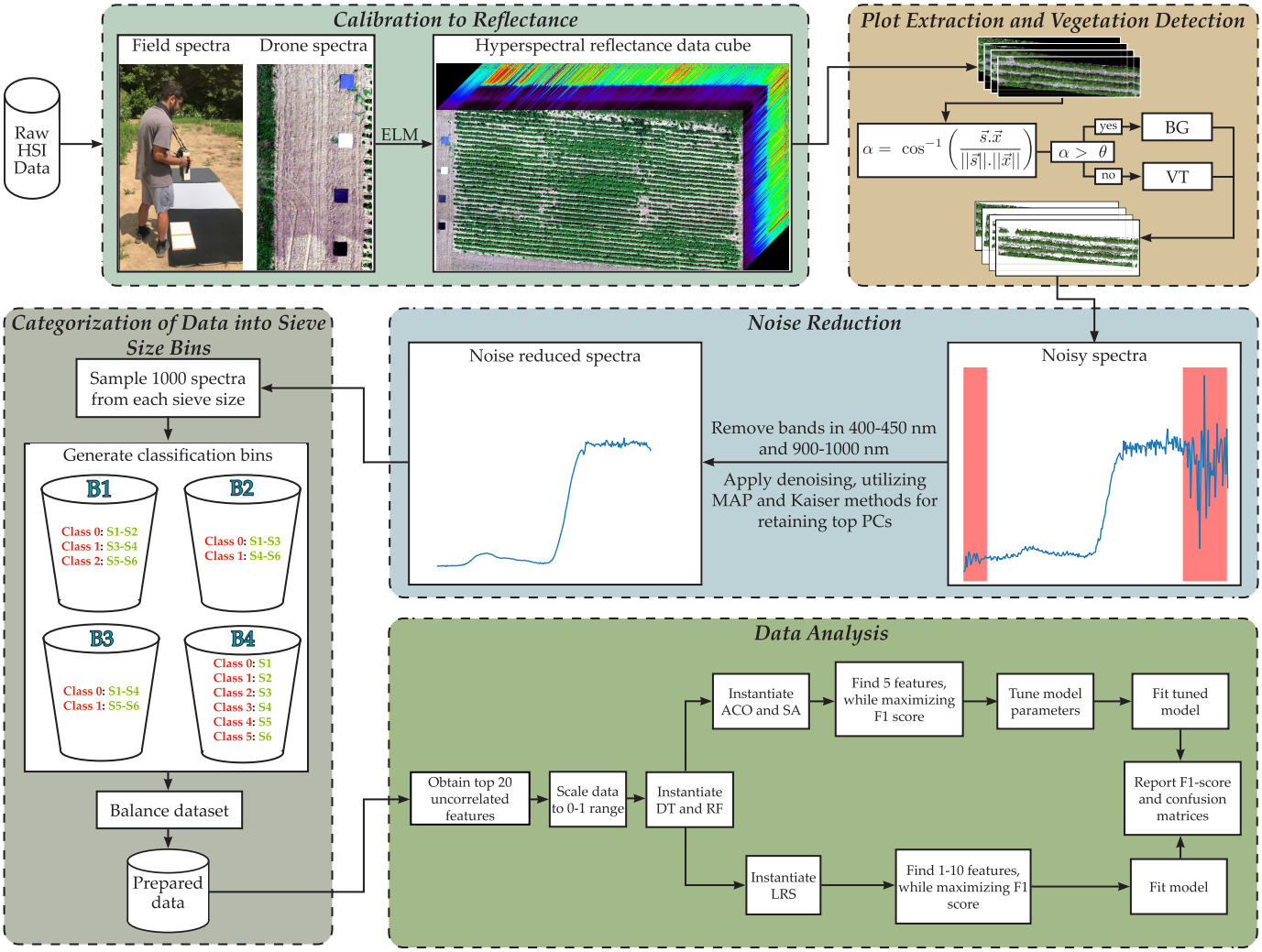

Fig. 3. Flowchart of the methods section from calibration to reflectance to data analysis. BG: background and VT: vegetation.

to the high-pass wavelet coefficients as follows:

$$d_{j,k} = d_{j,k}\ \max\left(0, \left(1 - \frac{\text{thr}^2}{S_{j,k}^2}\right)\right) \tag{1}$$

where $d_{j,k}$ is the jth wavelet coefficient of size k, $S_{i,j}^2 = (|d_{j,k-1}|^2 + |d_{j,k}|^2 + |d_{j,k+1}|^2)/3$ is the average d_j window with size three centering at k, $\text{thr} = (2\sigma_n^2 \log\ n)^{1/2}$ is the universal threshold, and σ is the noise approximate [13], [26]. Prior to passing the clean spectra to the final analysis stage, data were prepared for analysis.

4) Categorization of Data Into Sieve Size Bins: A thousand spectra from each noise-free, vegetation sieve size class were randomly sampled, to accelerate training. Consequently, four different classification bins, B1–B4, were organized for the final objective: B1 for determining the classification performance between $S1 - S2$, $S3 - S4$, and $S5 - S6$ ($\text{class}_0 = S1 - S2$, $\text{class}_1 = S3 - S4$, and $\text{class}_2 = S5 - S6$); B2 for assessing separation between $S1 - S3$ and $S4 - S6$ ($\text{class}_0 = S1 - S3$ and $\text{class}_1 = S4 - S6$); B3 for investigating classification efficiency between $S1 - S4$ and $S5 - S6$ ($\text{class}_0 = S1 - S4$ and $\text{class}_1 = S5 - S6$); and B4 for evaluating separation between each sieve size ($\text{class}_0 = S1$, $\text{class}_1 = S2$, $\text{class}_2 = S3$, $\text{class}_3 = S4$, $\text{class}_4 = S5$, and $\text{class}_5 = S6$). The above information is schematically depicted in Fig. 3. It should be noted that the 2020 data lacked $S6$ for all cultivars; thus, the B4 would accordingly change to distinguish between $S1 - S4$ and $S5$. We avoided changing the naming of the sieve size bins hereafter. Finally, data bins were balanced being passed to the data analysis step.

5) Data Analysis: The first step of the data analysis stage is data decorrelation, followed by normalization. The top-20 decorrelated features were retained and scaled to a 0–1 range. The reason for selecting top-20 decorrelated features (based on Pearson's correlation coefficient, in the descending order), and not performing subsetting via thresholding per Pearson's correlation coefficient, was to ensure that the selection process occurred uniformly across different data bins (i.e., features are being drawn from independent variables populations of the same size). In this study, we utilized random forests (RF) and decision tree (DT) classifiers for our classification objective. For each data bin, a ratio of 70%–30% was used for training and testing splits, in a stratified-random fashion.

TABLE II
OPTIMIZATION MODELS, CORRESPONDING PARAMETERS, AND ASSOCIATED VALUE RANGES AS IDENTIFIED FOR HYPERPARAMETER TUNING

Optimization Model	Hyperparameter	Title	Range
ACO	α	Information elicitation factor	$10^{-5} - 0.5$
	ρ	Pheromone evaporation coefficient	$10^{-5} - 0.5$
	τ_0	Initial pheromone intensity	$10^{-5} - 1$
	Q	Pheromone intensity	$10^{-5} - 1$
	N_{ant}	Number of ants	$20 - 200$
	β	Meta-heuristic factor	$1 - 5$
SA	α	Cooling factor	$0.8 - 0.99$
	T_0	Initial temperature	$10^{-1} - 500$
	$N_{iter-sub}$	Number of sub-iterations	$20 - 200$

Next, we used our previously published feature selection library (Jostar [24]). ACO and SA optimization algorithms, embedded in Jostar, were utilized to detect only five differentiating features, while Plus-l Minus-R (LRS) was used to identify one to ten features while maximizing the F1 score [50]. ACO and SA models' parameters were tuned for 200 iterations prior to running the final model (see Table II), and the LRS method's parameters were set to $L = 3$ and $R = 2$, thus, without a need for hyperparameter tuning. We opt to maximize the F1 score for all classification tasks since the F1 score takes into account the impact of both precision and recall and, thus, is easier to interpret compared to examining two metrics separately (i.e., precision and recall). The F-1 score, confusion matrices, and ROC curves were reported.

E. Comparison With VIs

Finally, in order to prove the robustness and reliability of the proposed approach, we compared our results with eight most commonly used narrowband VIs, namely, enhanced VI (EVI), green chlorophyll index (CI_{green}), red edge chlorophyll index ($CI_{Red\ Edge}$), normalized difference VI (NDVI), normalized difference red edge index (NDRE), photochemical reflectance index (PRI), ratio VI (PRI), and the visible atmospherically resistant index (VARI). Depicted in Table III is the stated VIS along with their formula. The mentioned VIs were only ran for comparison with the best performing model between ACO and SA (five features only), across the three mentioned datasets (i.e., 2019, 2020, and 2019-2020).

F. Software

ENVI software (version 5.4) was used for calibration to reflectance. The feature selection library, Jostar (https://github.com/amirhszd/jostar [24]), was employed in Python 3.6 [61], while the Scikit-learn library was utilized for RF and DT classifiers [48].

III. RESULTS

The results section is divided into three subsections: 1) the descriptive analysis provides information on normality assessment and correlation evaluation between features; 2) the results for ACO and SA optimization models, identifying only five features, are presented; and 3) results for the LRS optimization model, exploring the choice of one to ten features from the given space, are provided.

TABLE III
NARROWBAND VIS FOR POD MATURITY ASSESSMENT OF SNAP BEAN

Vegetation Index	Formula	Reference
EVI	$2.5[(\lambda_{800} - \lambda_{670})/(\lambda_{800} - 6\lambda_{670} - 7.5\lambda_{475} + 1)]$	[27]
CI_{green}	$\lambda_{780}/\lambda_{550}$ - 1	[19]
$CI_{Red\ Edge}$	$\lambda_{800}/\lambda_{740}$ - 1	[38]
NDVI	$(\lambda_{850} - \lambda_{675})/(\lambda_{850} + \lambda_{675})$	[9]
NDRE	$(\lambda_{790} - \lambda_{720})/(\lambda_{790} + \lambda_{720})$	[15]
PRI	$(\lambda_{531} - \lambda_{570})/(\lambda_{531} + \lambda_{570})$	[16]
RVI	$\lambda_{790}/\lambda_{670}$	[30]
VARI	$(\lambda_{550} - \lambda_{660})/(\lambda_{550} + \lambda_{660} - \lambda_{470})$	[19]

A. Descriptive Analysis

Normality and correlation analyses were performed, on each data collection day, after noise removal, to develop a robust approach that can reliably be based on either parametric or nonparametric methods. We chose to depict correlation and normality results for the last flight collection day of each dataset since test results were similar across dates (see Fig. 4). It can be observed from the correlation matrices that spectral features that are far apart in terms of wavelength are exhibited lower correlations, as expected; see, for example, 450–550 nm with 750–900 nm and 600–725 nm with 750–900 nm. A graphical evaluation of Q–Q plots of 2019 and 2020 datasets showed that both datasets are entirely multivariate nonnormal.

Table IV presents plot sieve size counts for the 2019 and 2020 datasets. It can be seen that the 2020 dataset was higher in number for sieve size 5 but lower for sieve sizes 2 and 3. This substantial discrepancy was ascribed to different flight plans during the respective seasons, as flights occurred when the illumination conditions were uniform, with an accompanying low chance of precipitation.

B. ACO and SA

1) 2019 Data Results: Results for five selected features for all models and sieve size bins are depicted in Fig. 5. The Kaiser denoising approach outperformed the MAP denoising approach in all cases, for both ACO and SA optimization models. Looking at Fig. 5(b), we can see that the RF model outperformed DT, with the highest performing accuracy of F1 = 0.85 for $B3$, with $B2$ next with F1 = 0.77, and the lowest accuracy of F1 = 0.30 for $B4$. The $B3$ test bin arguably is most useful for differentiating between ready-to-harvest and not ready-to-harvest in the case of the large cultivars

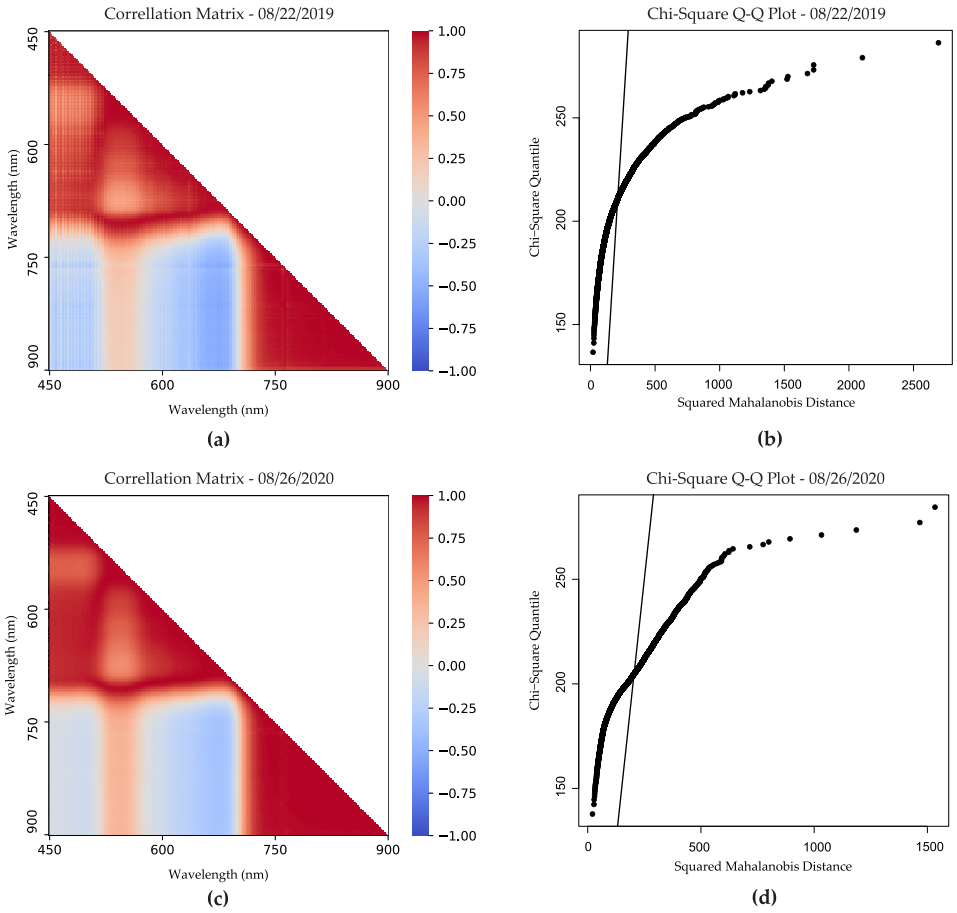

Fig. 4. Correlation matrices and Q–Q normality plots for (a) and (b) 2019 and (c) and (d) 2020 datasets on the final flight dates for each season.

(Venture and Huntington). The results from $B2$ proved to be more inclusive, determining ready-to-harvest versus not ready-to-harvest, for both large cultivars (Venture and Huntington) and four sieve cultivars (Cabot and Colter). However, it should be noted that large cultivars are considered mature when they reach sieve sizes 5 and 6. The bagging of size 4 sieves along with 5 and 6, thus, resulted in a practical error when scheduling maturity for large cultivars.

We chose to depict confusion matrices for the test set of the most and least accurate performing optimization method, classifier, and denoising methods. Fig. 6 shows the confusion matrices for $RF\text{-}Kaiser\text{-}B3$ and $DT\text{-}MAP\text{-}B4$, via the SA model. It is clear from Fig. 6(a) that the distribution of error between classes was balanced, and the confusion matrix was highly diagonal, with an AUC of 0.91. Fig. 6(b), representing $DT\text{-}MAP\text{-}B4$ via the SA model, provides helpful insight regarding the distribution of errors between different classes (sieve sizes). It is evident that the confusion matrix could be divided into two smaller sections (i.e., square matrices), one encompassing class_0 to class_3 ($S1-S4$), and the other incorporating class_4 to class_5 ($S5-S6$), indicating that this problem could be distilled into a binary problem for maximum performance, further demonstrating why $B3$ outperformed other models. On another note, class_4 and class_5, corresponding to $S5$ and $S6$, respectively, were largely misclassified across these two classes, and the same was true for class_0 and class_1 corresponding to $S1$ and $S2$, respectively (i.e., the spread of error). However, class_2 and class_3, corresponding to $S3$ and $S4$, exhibited a wider spread in terms of error.

TABLE IV
PLOT SIEVE SIZE COUNTS FOR 2019 AND 2020 SNAP BEAN DATASETS

	Sieve Size					
	1	**2**	**3**	**4**	**5**	**6**
2019 plot count	19	19	12	29	6	7
2020 plot count	21	5	7	29	10	

Table V lists the identified wavelengths for the 2019 dataset for the best performing bin ($B3$). These wavelengths reside in the green, red, and near-infrared spectral regions with wavelengths at ∼530, ∼620, ∼660, ∼720, ∼740, and ∼760 nm. A number of the selected wavelengths, such as 759 and 766 nm, are in close proximity, thus a higher chance of them being correlated. This is not desirable in a commercial platform, and we believe that the algorithm could perform almost similarly with fewer than five bands, which is also why we approached this study with a two-level analysis, i.e., five features versus one to ten features.

2) 2020 Data Results: Fig. 7 shows results for five selected features across all models and sieve size bins. At first glance,

TABLE V

RESULTS FOR THE ACO AND SA 2019 DATASETS FOR FIVE SELECTED WAVELENGTHS AND THE BEST-PERFORMING SNAP BEAN SIEVE SIZE BIN ($B3$), DT AND RF, AND KAISER AND MAP DENOISING METHODS

Optimization Model	Classifier	Denoising Method	Identified Wavelengths (nm) 1	2	3	4	5	F1 Score
ACO	DT	Kaiser	532	657	699	717	766	0.81
	DT	MAP	528	663	717	728	766	0.80
	RF	Kaiser	657	717	721	759	766	0.84
	RF	MAP	663	708	721	739	766	0.83
SA	DT	Kaiser	512	532	657	717	766	0.81
	DT	MAP	521	528	621	717	766	0.80
	RF	Kaiser	532	621	717	737	766	0.85
	RF	MAP	663	708	721	739	766	0.83

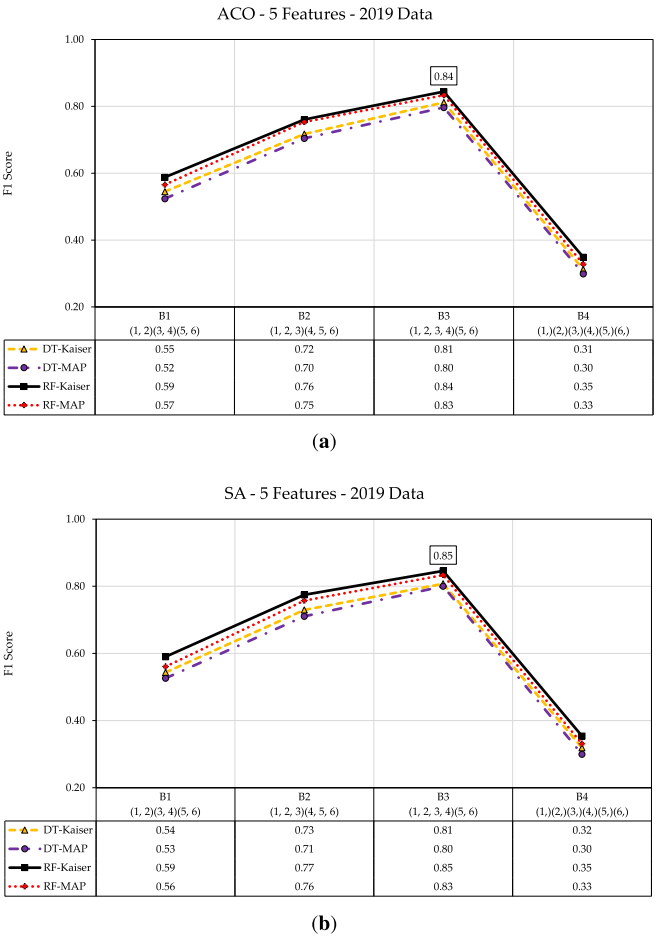

Fig. 5. (a) ACO and (b) SA 2019 dataset F1 score results for five selected features through ACO and SA optimization methods, for DT and RF classifiers, and Kaiser and MAP denoising methods, across four bins. Note that $B3$ outperforms others.

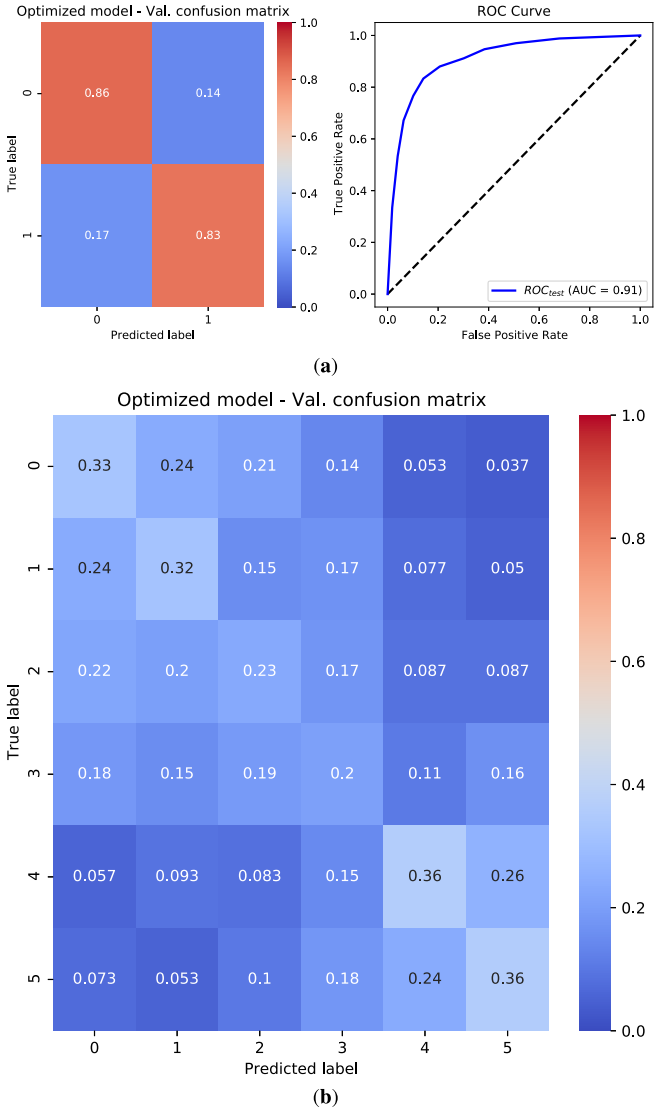

Fig. 6. ACO and SA 2019 dataset confusion matrices and ROC curve for five features on (a) $RF\text{-}Kaiser$ on $B3$ and (b) $DT - MAP$ on $B4$ both via the SA model.

it can be noted that the 2020 dataset outperformed the 2019 dataset. Results from both ACO and SA optimization models were similar, with SA marginally outperforming ACO in the $RF\text{-}Kaiser$ subsets. The SA-$RF\text{-}Kaiser\text{-}B3$ test set performed most accurate at F1 $=$ 0.91. These results again underscore the feasibility of the introduced algorithms for the maturity assessment of snap bean.

Fig. 8 shows the confusion matrix of the most accurate test set (SA-$RF\text{-}Kaiser\text{-}B3$) for the 2020 dataset. It is evident that class$_0$ or (1, 2, 3, 4) exhibited a lower error of omission than those of class$_1$ (6.7% compared to 12%). However, the overall ROC curve generated a superior AUC $=$ 0.96. Table VI demonstrates the five selected wavelengths for the best performing sieve size bin ($B3$) on the 2020 dataset. The

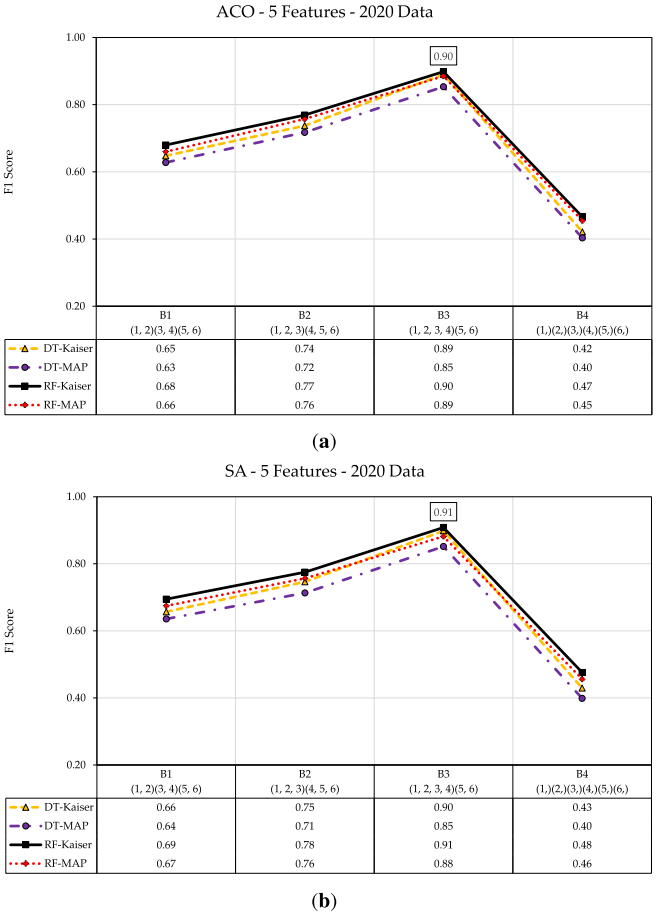

Fig. 7. ACO and SA 2020 dataset results for the F1 score for five identified wavelengths for DT and RF classifiers, and Kaiser and MAP denoising methods, across all four sieve size bins, for the 2020 dataset. Note that $B3$ outperformed other tests (sieve size bins).

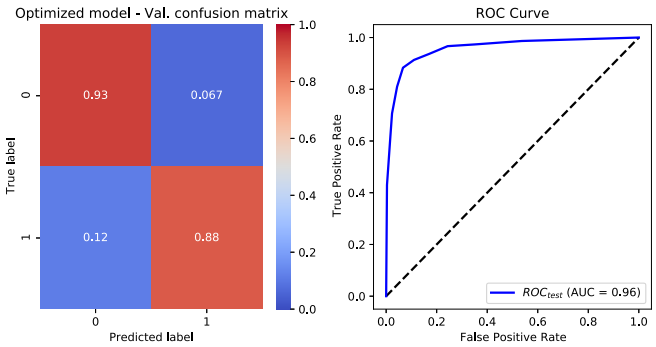

Fig. 8. ACO and SA 2020 dataset ROC and confusion matrix results for five identified wavelengths and the best performing test: $RF\text{-}Kaiser$ for the snap bean $B3$ sieve size bin via the SA model.

identified bands were located in the ∼450, ∼640, ∼720, ∼740, ∼760, and ∼850 nm spectral regions. The wavelength at 846 nm, only recurring in $RF\text{-}MAP$ tests, was not identified in the 2019 dataset.

3) 2019-2020 Data Results: The results for five selected features for the combined 2019-2020 dataset are presented in Fig. 9. The two combined datasets performed worse, in terms of accuracy, than when evaluated individually.

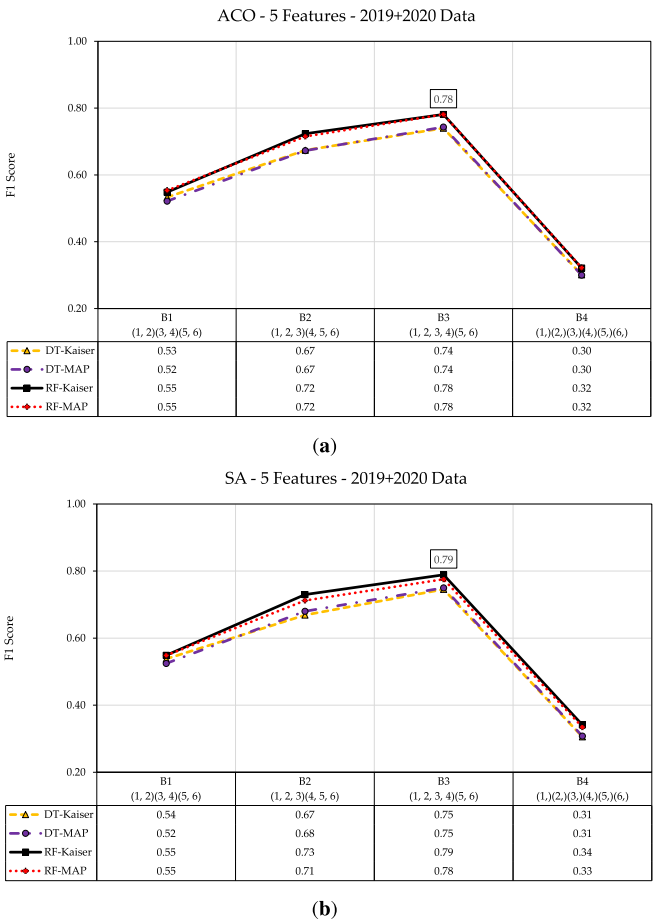

Fig. 9. (a) ACO and (b) SA 2019-2020 F1 score results for the five identified wavelengths via the ACO and SA methods for DT and RF classifiers, and Kaiser and MAP denoising methods for all four snap bean sieve size bins.

The best-performing model again was the SA-$RF\text{-}Kaiser\text{-}B3$ with F1 = 0.79.

Fig. 10 shows the confusion matrix and the ROC curve for the combined 2019-2020 dataset for the SA-$RF\text{-}Kaiser\text{-}B3$ test set, i.e., the most accurate results. There was a larger error of omission for class_1 or (5, 6) sieve sizes (27%) compared to class_0 or (1, 2, 3, 4) sieve sizes (16%). The ROC curve generated an AUC = 0.84 for this test, which deemed satisfactory. Table VII lists the selected wavelengths for the two optimization models (ACO and SA) across two classifiers and two denoising methods for the $B3$ sieve size bin. It is evident that wavelengths in ∼450, ∼530, ∼590, ∼620, ∼640, ∼720, ∼760, and ∼860 nm were recurrent. Wavelengths in the near-infrared region were repeated more frequently compared to those identified from each dataset separately.

C. LRS

1) 2019 Data Results: Table VIII shows the F1 score for the approach targetting one to ten selected wavelengths across all sieve size bins using DT and RF, via Kaiser and MAP denoising schemes. We observed that: 1) after a certain number of selected wavelengths, appending more wavelengths either improves the accuracy marginally or is detrimental to the

TABLE VI

RESULTS FOR THE ACO AND SA 2020 DATASETS FOR FIVE IDENTIFIED WAVELENGTHS AND THE BEST PERFORMING SNAP BEAN SIEVE SIZE BIN ($B3$) USING DT AND RF CLASSIFIERS, AND KAISER AND MAP DENOISING METHODS

Optimization Model	Classifier	Denoising Method	Identified Wavelengths (nm) 1	2	3	4	5	F1 Score
ACO	DT	Kaiser	646	715	737	759	766	0.89
	DT	MAP	452	712	721	744	766	0.85
	RF	Kaiser	452	715	730	759	766	0.90
	RF	MAP	646	717	759	766	846	0.89
SA	DT	Kaiser	646	715	737	759	766	0.90
	DT	MAP	452	521	706	717	759	0.85
	RF	Kaiser	452	528	715	759	766	0.91
	RF	MAP	646	717	744	759	846	0.88

TABLE VII

ACO AND SA 2019-2020 DATASETS FOR FIVE SELECTED WAVELENGTHS AND THE MOST ACCURATE SIEVE SIZE BIN, $B3$, USING DT AND RF CLASSIFIERS, AND KAISER AND MAP DENOISING METHODS

Optimization Model	Classifier	Denoising Method	Identified Wavelengths (nm) 1	2	3	4	5	F1 Score
ACO	DT	Kaiser	452	608	643	717	766	0.74
	DT	MAP	452	530	586	657	766	0.74
	RF	Kaiser	452	459	717	728	766	0.78
	RF	MAP	452	521	617	706	766	0.78
SA	DT	Kaiser	452	468	608	717	766	0.75
	DT	MAP	452	476	530	710	866	0.75
	RF	Kaiser	452	530	717	766	850	0.79
	RF	MAP	452	530	586	766	897	0.78

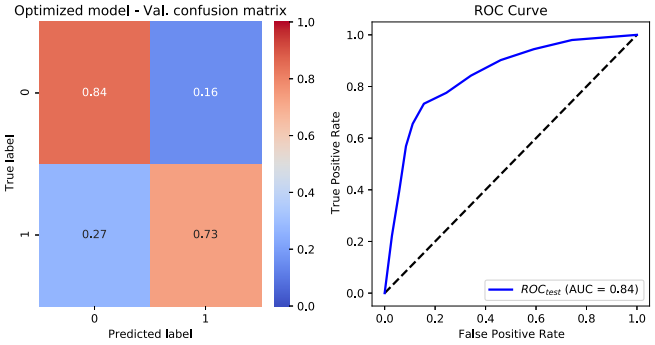

Fig. 10. ACO and SA 2019-2020 confusion matrix and ROC curve for five identified wavelengths for the best-performing test $RF\text{-}Kaiser$ on the $B3$ snap bean sieve size bin via the SA model.

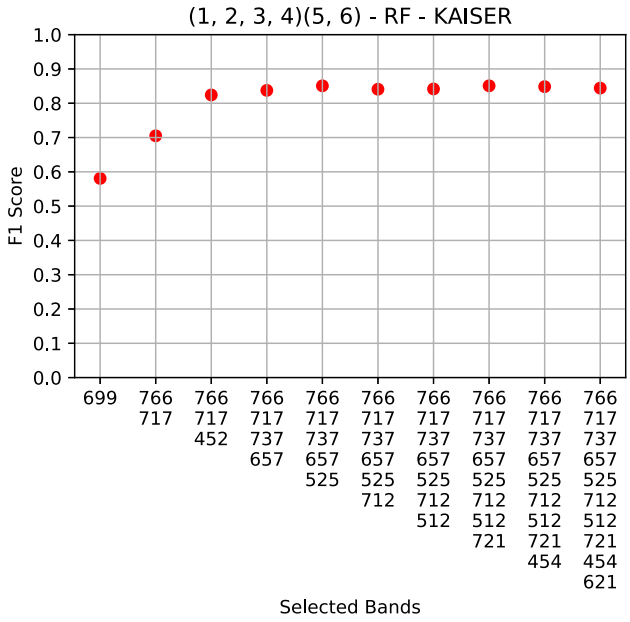

Fig. 11. LRS 2019 dataset Pareto frontier for one to ten selected bands on $RF\text{-}Kaiser\text{-}B3$. Notice the trivial improvement beyond four selected bands.

overall classification performance and 2) $RF\text{-}Kaiser$ outperformed other classifiers and denoising methods. Almost all tests started to plateau in accuracy when exceeding three to six selected wavelengths. We chose to depict the Pareto frontier of the most accurate test ($RF\text{-}Kaiser\text{-}B3$), along with the corresponding selected wavelengths in Fig. 11. As the number of wavelengths increased, the algorithms selected bands that potentially could be slightly correlated, thus the slight improvement in the F1 score; this was expected, as noted previously (see Section III-B1). Wavelengths for three and four selected features were found to be most discriminating, yet not in close spectral proximity. Three identified wavelengths at ~760, ~710, and ~450 nm proved discriminating with F1 = 0.82. Moreover, four wavelengths at ~766, ~720, ~740, and ~660 nm, with an F1 = 0.84, were found the most useful for differentiating the 2019 dataset. The corresponding confusion matrix for this test is depicted in Fig. 12, demonstrating a highly diagonal matrix with similar errors of omission for both classes, and a robust AUC = 0.90.

TABLE VIII

LRS 2019 DATASET F1 SCORES FOR ONE TO TEN SELECTED FEATURES ACROSS ALL TESTS. NOTICE THE VARIABLE (LIMITED) EFFECT ON THE PERFORMANCE BY ADDING FEATURES ABOVE THREE TO SIX BANDS

Bin	Classifier	Denoising Method	F1 score for N selected wavelengths									
			1	2	3	4	5	6	7	8	9	10
	DT	Kaiser	0.40	0.42	0.48	0.48	0.48	**0.53**	0.53	0.54	0.54	0.54
B1	DT	MAP	0.39	0.43	0.48	**0.50**	0.48	0.50	0.50	0.51	0.52	0.52
(1, 2)(3, 4)(5, 6)	RF	Kaiser	0.39	0.46	**0.57**	0.57	0.57	0.58	0.58	0.58	0.58	0.56
	RF	MAP	0.39	0.44	0.50	0.53	**0.55**	0.54	0.54	0.55	0.55	0.54
	DT	Kaiser	0.53	0.62	0.67	**0.71**	0.71	0.72	0.72	0.73	0.73	0.72
B2	DT	MAP	0.55	0.59	0.64	0.67	**0.69**	0.70	0.70	0.70	0.71	0.70
(1, 2, 3)(4, 5, 6)	RF	Kaiser	0.54	0.63	0.70	0.74	**0.76**	0.76	0.76	0.75	0.75	0.76
	RF	MAP	0.56	0.60	0.73	0.74	**0.75**	0.74	0.75	0.75	0.75	0.76
	DT	Kaiser	0.58	0.64	0.74	**0.79**	0.79	0.79	0.81	0.80	0.81	0.81
B3	DT	MAP	0.60	0.62	0.76	**0.79**	0.79	0.80	0.80	0.80	0.79	0.79
(1, 2, 3, 4)(5, 6)	RF	Kaiser	0.58	0.71	0.82	**0.84**	0.85	0.84	0.84	0.85	0.85	0.84
	RF	MAP	0.55	0.69	0.80	**0.82**	0.82	0.82	0.82	0.82	0.83	0.83
	DT	Kaiser	0.21	0.23	0.28	**0.30**	0.30	0.32	0.32	0.32	0.32	0.32
B4	DT	MAP	0.19	0.23	0.28	0.28	**0.30**	0.30	0.30	0.31	0.32	0.32
(1,)(2,)(3,)(4,)(5,)(6,)	RF	Kaiser	0.21	0.25	0.29	0.33	**0.34**	0.35	0.34	0.35	0.35	0.34
	RF	MAP	0.20	0.24	0.28	**0.31**	0.32	0.33	0.33	0.33	0.33	0.33

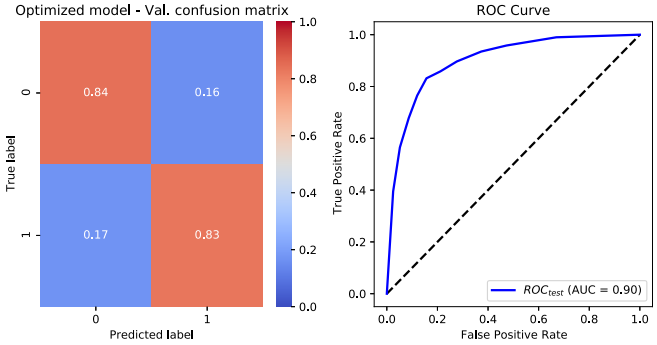

Fig. 12. LRS 2019 dataset confusion matrix for four selected bands on $RF\text{-}Kaiser\text{-}B3$.

2) 2020 Data Results: Table IX shows the F1 score results for the 2020 data when selecting one to ten wavelengths. It is evident that, beyond four to six wavelengths, the algorithm performance either decreased or increased minimally. The best-performing model was $RF\text{-}Kaiser\text{-}B3$ with F1 = 0.91 at five selected wavelengths. Fig. 13 displays the Pareto frontier for the best performing model ($RF\text{-}Kaiser\text{-}B3$) over the number of bands selected. It can be observed that the model built upon three highly uncorrelated wavelengths, i.e., ∼760, ∼715, and ∼452 nm, with F1 = 0.87, up to five wavelengths, after which the performance plateaued. The identified five wavelengths were ∼760, ∼715, ∼450, and ∼740 nm. The confusion matrix and the ROC curve for the best performing model ($RF\text{-}Kaiser\text{-}B3$) on five selected wavelengths are depicted in Fig. 14. We can see that the confusion matrix and the ROC curve are somewhat similar to those in Fig. 8. There is a larger error of omission for the class_1 compared to class_0 (0.12 versus 0.057) along with an overall robust AUC = 0.97.

3) 2019-2020 Data Results: Table X shows the 2019-2020 dataset F1 score results for one to ten selected bands. Similar to results reported for the 2020 dataset, above three to six

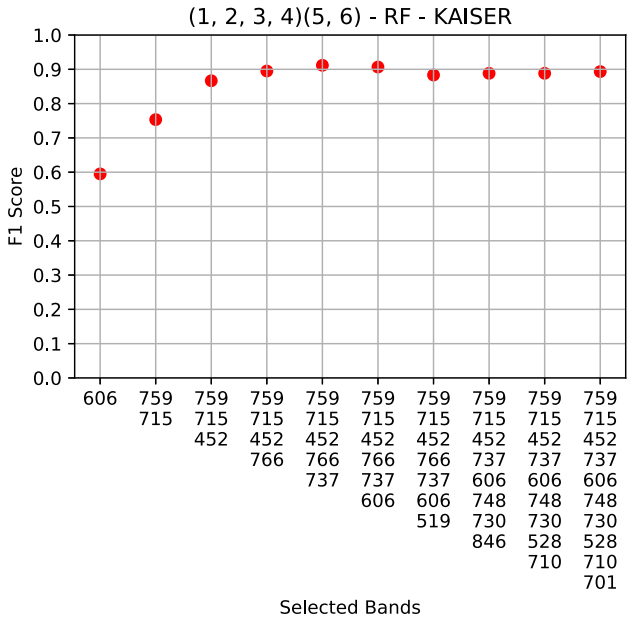

Fig. 13. LRS 2020 dataset Pareto frontier for one to ten selected bands on $RF\text{-}Kaiser\text{-}B3$. Note the drop in accuracy beyond five selected bands.

wavelengths, the performance plateaued. The most accurate test ($RF\text{-}Kaiser\text{-}B3$) exhibited an F1 = 0.77 with only four selected bands. Fig. 15 depicts the Pareto frontier curve of the best performing model ($RF\text{-}Kaiser\text{-}B3$). It is observable that three and four wavelengths are points at which the curve starts to plateau, with selected wavelengths at ∼700, ∼760, ∼660, ∼700, ∼760, ∼660, and ∼640 nm, with F1 = 0.75 and 0.77, respectively. Moreover, the overall accuracy measures using the LRS method were somewhat lower than those found via SA [0.77 versus 0.79; see Fig. 9(b)]. The confusion matrix is diagonal, and the ROC curve shows an AUC = 0.84 (see Fig. 16).

TABLE IX

LRS 2020 DATASET F1 SCORES FOR ONE TO TEN SELECTED FEATURES. NOTICE THE VARIABLE (LIMITED) PERFORMANCE IN BANDS ABOVE THREE TO SIX

Bin	Classifier	Denoising Method	F1 score for N selected wavelengths									
			1	2	3	4	5	6	7	8	9	10
	DT	Kaiser	0.40	0.44	0.56	**0.64**	0.62	0.65	0.65	0.67	0.64	0.66
B1	DT	MAP	0.39	0.48	0.53	0.59	0.61	**0.63**	0.63	0.62	0.63	0.63
(1, 2)(3, 4)(5, 6)	RF	Kaiser	0.34	0.56	0.66	0.66	**0.67**	0.68	0.65	0.67	0.68	0.67
	RF	MAP	0.39	0.48	0.64	**0.65**	0.65	0.66	0.67	0.65	0.67	0.66
	DT	Kaiser	0.54	0.62	0.70	0.72	**0.73**	0.73	0.73	0.73	0.74	0.74
B2	DT	MAP	0.55	0.62	0.65	0.69	0.70	**0.72**	0.73	0.73	0.73	0.73
(1, 2, 3)(4, 5, 6)	RF	Kaiser	0.55	0.63	0.73	**0.75**	0.75	0.76	0.76	0.76	0.76	0.76
	RF	MAP	0.56	0.65	0.72	**0.74**	0.74	0.75	0.74	0.76	0.76	0.75
	DT	Kaiser	0.60	0.69	0.82	**0.84**	0.85	0.87	0.88	0.88	0.87	0.88
B3	DT	MAP	0.56	0.75	0.82	**0.84**	0.84	0.84	0.84	0.84	0.84	0.84
(1, 2, 3, 4)(5, 6)	RF	Kaiser	0.60	0.75	0.87	0.90	**0.91**	0.91	0.88	0.89	0.89	0.89
	RF	MAP	0.57	0.76	0.82	0.84	**0.86**	0.86	0.86	0.86	0.87	0.88
	DT	Kaiser	0.23	0.28	0.37	**0.39**	0.39	0.39	0.41	0.41	0.41	0.40
B4	DT	MAP	0.23	0.27	0.30	0.36	**0.37**	0.38	0.39	0.39	0.39	0.40
(1,)(2,)(3,)(4,)(5,)(6,)	RF	Kaiser	0.23	0.29	0.37	0.43	**0.45**	0.45	0.44	0.45	0.45	0.45
	RF	MAP	0.23	0.33	0.41	**0.44**	0.44	0.44	0.45	0.44	0.45	0.45

TABLE X

LRS 2019-2020 DATASET F1 SCORES FOR ONE TO TEN IDENTIFIED FEATURES FOR ALL TESTS. NOTE THE VARIABLE (LIMITED) INFLUENCE ON THE ACCURACY METRIC BY APPENDING FEATURES ABOVE THREE TO SIX BANDS

Bin	Classifier	Denoising Method	F1 score for N selected wavelengths									
			1	2	3	4	5	6	7	8	9	10
	DT	Kaiser	0.38	0.42	0.45	0.48	**0.50**	0.50	0.50	0.52	0.53	0.54
B1	DT	MAP	0.38	0.40	0.48	**0.51**	0.49	0.51	0.53	0.51	0.52	0.51
(1, 2)(3, 4)(5, 6)	RF	Kaiser	0.38	0.43	0.53	0.54	**0.56**	0.56	0.56	0.55	0.55	0.56
	RF	MAP	0.38	0.45	0.53	**0.54**	0.54	0.53	0.53	0.53	0.55	0.55
	DT	Kaiser	0.54	0.58	0.62	0.63	**0.65**	0.66	0.66	0.64	0.66	0.65
B2	DT	MAP	0.53	0.57	0.62	0.63	**0.65**	0.65	0.65	0.66	0.65	0.65
(1, 2, 3)(4, 5, 6)	RF	Kaiser	0.54	0.62	0.68	**0.70**	0.71	0.71	0.71	0.73	0.72	0.73
	RF	MAP	0.54	0.58	0.67	0.68	**0.69**	0.69	0.69	0.68	0.70	0.70
	DT	Kaiser	0.58	0.67	0.72	0.74	**0.75**	0.75	0.74	0.75	0.76	0.75
B3	DT	MAP	0.59	0.64	0.68	**0.73**	0.73	0.72	0.74	0.75	0.75	0.76
(1, 2, 3, 4)(5, 6)	RF	Kaiser	0.58	0.65	0.75	**0.77**	0.77	0.78	0.77	0.77	0.76	0.79
	RF	MAP	0.58	0.69	**0.75**	0.75	0.76	0.78	0.78	0.78	0.78	0.77
	DT	Kaiser	0.21	0.22	0.23	**0.27**	0.27	0.29	0.28	0.29	0.28	0.29
B4	DT	MAP	0.21	0.23	0.24	0.26	**0.29**	0.29	0.30	0.30	0.31	0.29
(1,)(2,)(3,)(4,)(5,)(6,)	RF	Kaiser	0.21	0.24	0.29	0.29	0.32	**0.35**	0.33	0.34	0.34	0.35
	RF	MAP	0.22	0.24	0.29	**0.31**	0.31	0.32	0.31	0.31	0.33	0.34

D. Comparison With VIs

The findings of this research, for the most accurate test ($RF\text{-}Kaiser\text{-}B3$) via SA for five identified wavelengths, for all three datasets (2019, 2020, and 2019-2020) were compared with eight commonly used VIs (as referenced in Table III) and tabulated in Table XI. As can be seen, our suggested methodology outperformed all VIs for all three datasets, which further proves the importance and contribution of a robust framework.

IV. DISCUSSION

The major findings of this study included identification of wavelengths corresponding to accurate snap bean pod maturity assessment, detecting various sieve size classes (bins), and their accuracy performance. These results are useful for operational, multispectral sensor design, specifying ideal sieve sizes that can be discriminated, and the expected accuracies of resultant classifications, respectively.

The variability in accuracy measures (F1 score) for the three datasets requires more scrutiny. As we saw in Section III, the 2020 dataset delivered the most accurate F1 $= 0.91$ compared to 2019 (F1 $= 0.85$) and 2019-2020 (F1 $= 0.79$). We contend this inconsistency could be attributed to three factors. First, the 2019 dataset took advantage of a three-point ELM approach, while the 2020 dataset utilized a four-point ELM approach. This difference in the calibration-to-reflectance approach may have influenced the distinction between classes, i.e., the

TABLE XI

COMPARISON OF THE RESULTS, IN TERMS OF ACCURACY METRIC (F1 SCORE), FROM THE INTRODUCED FRAMEWORK, FOR THE MOST ACCURATE TEST (*RF-Kaiser-B3*) VIA SA FOR FIVE IDENTIFIED WAVELENGTHS, WITH EIGHT COMMONLY USED VIS

Data Set	F1 score								
	EVI	CI_{green}	$CI_{Red\ Edge}$	NDVI	NDRE	PRI	RVI	VARI	Jostar (ours)
2019	0.56	0.60	0.63	0.53	0.61	0.52	0.54	0.50	**0.85**
2020	0.56	0.65	0.60	0.58	0.67	0.48	0.58	0.54	**0.91**
2019-2020	0.51	0.58	0.60	0.54	0.61	0.48	0.52	0.46	**0.79**

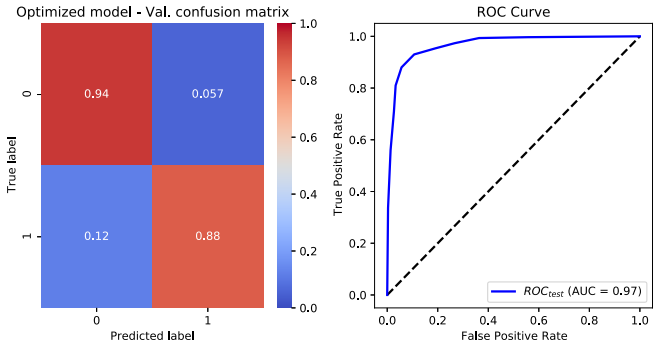

Fig. 14. LRS 2020 dataset confusion matrix for five selected bands on *RF-Kaiser-B3*.

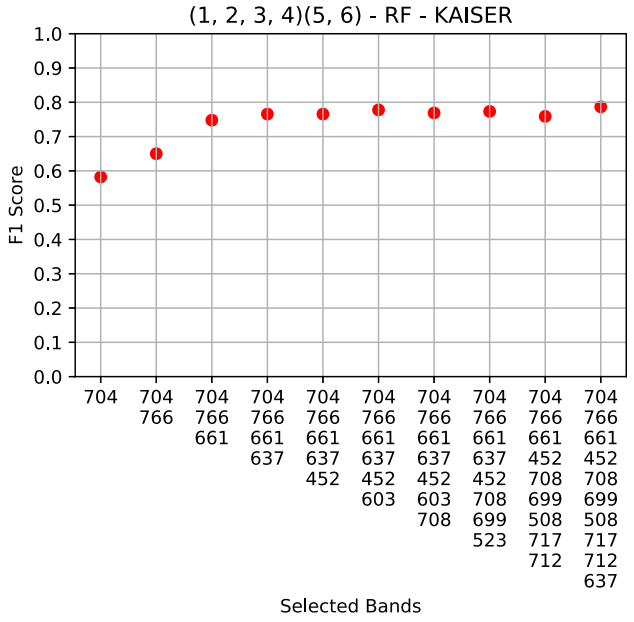

Fig. 15. LRS 2019-2020 dataset Pareto frontier for one to ten selected bands on *RF-Kaiser-B3*. Note the slight, inconsistent improvement in accuracy above four selected bands.

four-point ELM approached positively impacting the performance. Second, the 2020 dataset contained sieve sizes 1–5, while the 2019 dataset was comprised of sieve sizes 1–6. This dissimilarity between sieve size bins, in the 2020 data and the 2019 dataset, especially in the *B3* sieve size bin, could have led to a reduction in the complexity of the classification

TABLE XII

IDENTIFIED WAVELENGTHS ACROSS THE MOST ACCURATE TEST (*Kaiser-B3*) FOR READY-TO-HARVEST VERSUS NOT READY-TO-HARVEST CLASSIFICATION

Optimization Model	Data Set	Identified Wavelengths (nm)				
SA	2019	532	621	717	737	766
	2020	452	528	715	759	766
	2019-2020	452	530	717	766	850
LRS	2019		657	717	767	766
	2020	452	715	737	759	766
	2019-2020		637	661	704	766

problem and have increased the performance. Finally, the 2020 dataset identified a wavelength in the ∼450 nm spectral region as distinguishing, for multiple instances of the ACO, SA, and LRS methods (see Fig. 13), while the 2019 dataset did not detect this wavelength for ACO and SA, and only identified in this region for LRS in some instances (see Fig. 11). We believe that this wavelength could play a major role in pod maturity assessment since it recurred multiple times in tests. Also, we suspect that the drop in accuracy for the combined 2019-2020 dataset could be due to either the discrepancy in the ELM approach between 2019 and 2020 datasets or the simple fact that the model is generalizing. Future work should include an evaluation of the effect of the number of calibration panels in the ELM approach in order to increase the certainty around such factors. The identified wavelengths and their corresponding physiological links will be discussed next.

Tabulated in Table XII are recurring wavelengths from the SA and the LRS model, for the *Kaiser-B3* combination (the most accurate results). It is evident that repetitive wavelengths are present across all datasets, including ∼450, ∼530, ∼660, 700–720, ∼740, and ∼760 nm. An increased importance, thus, has been attributed to the red-edge region and its influence on the performance (see Figs. 11, 13, and 15). The identified regions were located in the blue, green, and red reflective regions, along with three bands in the red-edge region, with physiological links to chlorophyll density and plant health and vigor [12], [64]. Two of the major findings of this study, thus, are that the selected bands in the red-edge region were uncorrelated, while their addition to the band subset improved the overall test accuracy, i.e., an accurate model that was not overfitting (see Figs. 11, 13, and 15). In addition, we showed in-depth results for the best-performing sieve size bin (*B3*; [1, 2, 3, 4][5, 6]). This sieve size bin in effect creates

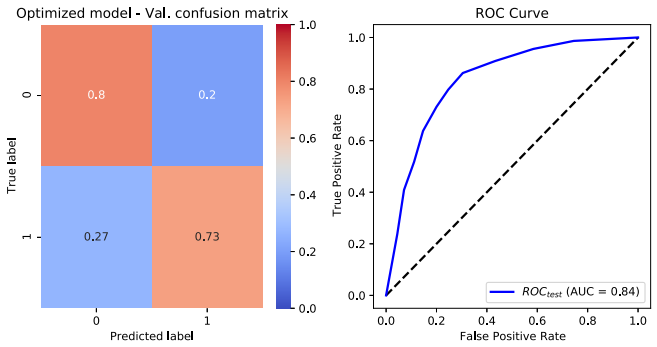

Fig. 16. LRS 2019-2020 dataset confusion matrix for four selected bands on $RF\text{-}Kaiser\text{-}B3$.

a ready-to-harvest versus not ready-to-harvest separation between the sieve sizes 1–4 and 5–6. The separation between the mentioned sieve sizes arguably is best suited for pod maturity assessment of large-sieve cultivars (Venture and Huntington). In other words, we demonstrated that pod maturity assessment of large-sieve cultivars is feasible, while cultivars with smaller sieve-size pods are harder to discriminate between (possibly due to a lack of spectral features between smaller sized pods; i.e., sieve sizes 1–4), when it comes to classification between ready-to-harvest and not ready-to-harvest snap bean [see Fig. 6(b)]. Finally, we compared the results of our approach for the best performing test ($RF\text{-}Kaiser\text{-}B3$) on SA with eight commonly used VIs, for which our results outperformed all.

Finally, the identified wavelengths or spectral regions (i.e., ∼450, ∼530, ∼660, 700–720, ∼740, and ∼760 nm) are similar to those detected in our previous study, for snap bean yield assessment via UAS [24] with identified wavelengths in ∼450, ∼500, ∼520, ∼650, ∼710, and ∼760 nm domains, as well as growth stage classification of snap bean in a greenhouse environment, with wavelengths in ∼500, ∼550, ∼660, and 720-740 nm regions [22]. We regard this as a significant result since in theory that one can evaluate both yield and pod maturity with a single, well-designed multispectral sensor that houses the identified wavelengths. The identified narrowband regions, recurring in all datasets, could be used to transfer the concepts learned into a more operational, affordable, and tunable multispectral system. One example of such a system is Tetracam's Micro-MCA (Chatsworth, CA, USA) with six tunable bands in the VNIR region. We contend that the next phase of application-specific, UAS-based precision agriculture will require such operational, tunable multispectral systems to improve algorithm performance on an application-by-application basis, as opposed to relying on hard-coded wavelengths on mass-produced imagers.

V. Conclusion

Accurate and timely pod maturity assessment of crops could contribute to a reduction in food waste while optimizing crop quality and quantity. We conducted a comprehensive pod maturity assessment of snap bean, as a proxy crop, across two years' worth of data, for two geographical locations, and six different cultivars via hyperspectral data captured using a UAS. To the best of our knowledge, this study is the first of its sort in terms of crop and sensing modality. The specific objectives of this research were to: 1) detect distinguishing spectral features using feature selection methods, explaining the separation between sieve size classes and 2) assess the viability of utilizing machine learning algorithms for classification of pod maturity sizes, for the snap bean as a proxy crop. The UAS hyperspectral data were collected over the summer of 2019 and 2020 in the VNIR domain (VNIR; 400–1000 nm), comprising 272 contiguous spectral bands. Ground-truth data, explaining snap bean pod maturity, were collected for six sieve size classes ($S1$–$S6$). We approached this study by first calibrating the collected raw spectra to reflectance using ELM, plot and vegetation extraction, noise reduction, categorization of data into sieve size bins, and data analysis. The noise reduction stage was a two-step process, starting with removing bands at the two ends of the collected spectra due to a lower SNR compared to regions at the center of the detector's response (higher sensor sensitivity) and then implementing a previously published approach, which exploited PCA and dual-tree complex wavelet transform for reducing noise. The captured ground-truth data in sieve sizes were used to create four classification bins, namely, $B1$ for evaluating separation between each sieve size; $B2$ for assessing separation between $S1-S3$ and $S4-S6$; $B3$ for evaluating classification performance between $S1-S2$, $S3-S4$, and $S5-S6$; and $B4$ for investigating separation performance between $S1-S4$ and $S5-S6$. We balanced the data (in terms of classes in each bin) and divided it into 70% training and 30% test set, in a stratified fashion, prior to setting up classification bins for data analysis. The data analysis stage included using our previously published feature selection library, "Jostar" [24], and utilized ACO and SA to detect the top five discriminating features, and Plus-L Minus-R (LRS) for identifying one to ten features. This study took advantage of RFs and DT as classifiers.

The findings of this study revealed that growth stage pod maturity assessment of snap bean can be performed accurately (F1 = 0.79–0.91) for large-sieve cultivars (e.g., Huntington and Venture) when classifying between ready-to-harvest versus not ready-to-harvest since there are distinct spectral features separating these two pod maturity categories. In other words, pod maturity classification for four-sieve and whole bean cultivars is not possible via imaging spectroscopy since there are not sufficient spectral features that could separate pods with smaller sieve sizes. SA outperformed ACO, RF showed superior performance compared to DT, and higher accuracies were observed for the Kaiser method when it came to retaining the top-K PCs. Results from the LRS optimization method showed that three to six spectral features were sufficient for robust classification performance.

Another major finding of this study was the identified wavelengths for pod maturity classification. Detected wavelengths across optimization models showed that recurring wavelengths resided in ∼450, ∼530, ∼660, 700–720, ∼740, and ∼760 nm spectral regions. These wavelengths were similar to those identified in our previously published study for yield assessment of snap bean crop via UAV (see [24]; detected wavelengths in this study were ∼450, ∼500, ∼520, ∼650, ∼710, and ∼760 nm), as well as our initial published study for

growth pod maturity assessment in a greenhouse environment (see [22]; ∼500, ∼550, ∼660, and 720–740 nm). This key finding implies that one could target both yield and pod maturity assessment of snap bean with a single multispectral sensor, given that it contains the selected spectral bands, while also confirming that the scaling of the conveyed notions from a greenhouse environment [22] to an airborne modality is practical. However, future work research is required to test these outcomes against other scenarios, e.g., climate variability, and to transfer the learned concepts into the operational multispectral realm, especially in terms of evaluating the impact of image calibration approaches.

Specifically, although this study spanned two geographical locations, two years of data, and six cultivars of snap beans, there are some limitations that need to be addressed. First, the hyperspectral imager contains inherent noise, which was not quantified. This mandates further research into evaluating noise (e.g., using an integrating sphere) and creating a baseline to compare the noise-reduced data against. Second, both geographical locations were situated in upstate New York. Future efforts should include incorporating data from geographical locations with different climates.

This study does, however, bode well for the extension of such results into the operational domain. Imaging spectrometers typically are costly to acquire and operate, thus limiting them to research environments. Our results show that one can distill a large number of wavelengths into a subset that can be designed into a multispectral, affordable, and operational UAS-based imaging system. Such a system now can be used in the context of a specific precision agriculture application, in this case, that of identifying the optimal harvest schedule for the snap bean.

ACKNOWLEDGMENT

The authors would like to thank Nina Raqueno and Tim Bauch, from the Center for Imaging Science's Data Acquisition Team, and Julie Kikkert, James Ballerstein, and Michael Rosato, from Cornell University, for their time and effort. They also appreciate the reviewers' feedbacks and the editor's constructive comments to improve the quality of this manuscript.

REFERENCES

[1] *United States Department of Agriculture*, USDA, Data Services. [Online]. Available: https://www.nass.usda.gov/Statistics_by_Subject/result.php?C1767500-2143-3B1C-80FA-FE88F6BB9E27§or=CROPS&group=VEGETABLES&comm=BEANS

[2] H. K. Aggarwal and A. Majumdar, "Hyperspectral image denoising using spatio-spectral total variation," *IEEE Geosci. Remote Sens. Lett.*, vol. 13, no. 3, pp. 442–446, Mar. 2016.

[3] D. W. Aha and R. L. Bankert, "A comparative evaluation of sequential feature selection algorithms," in *Learning From Data*. New York, NY, USA: Springer, 1996, pp. 199–206.

[4] M. L. Amodio, I. Capotorto, M. M. A. Chaudhry, and G. Colelli, "The use of hyperspectral imaging to predict the distribution of internal constituents and to classify edible fennel heads based on the harvest time," *Comput. Electron. Agricult.*, vol. 134, pp. 1–10, Mar. 2017.

[5] T. Amoriello, R. Ciccoritti, M. Paliotta, and K. Carbone, "Classification and prediction of early-to-late ripening apricot quality using spectroscopic techniques combined with chemometric tools," *Sci. Horticulturae*, vol. 240, pp. 310–317, Oct. 2018.

[6] G. A. Baker, L. C. Gray, M. J. Harwood, T. J. Osland, and J. B. C. Tooley, "On-farm food loss in northern and central California: Results of field survey measurements," *Resour., Conservation Recycling*, vol. 149, pp. 541–549, Oct. 2019.

[7] R. Battiti, "Using mutual information for selecting features in supervised neural net learning," *IEEE Trans. Neural Netw.*, vol. 5, no. 4, pp. 537–550, Jul. 1994.

[8] J. Benesty, J. Chen, Y. Huang, and I. Cohen, "Pearson correlation coefficient," in *Noise Reduction Speech Processing*. Berlin, Germany: Springer, 2009, pp. 1–4.

[9] T. N. Carlson and D. A. Ripley, "On the relation between ndvi, fractional vegetation cover, and leaf area index," *Remote Sens. Environ.*, vol. 62, no. 3, pp. 241–252, 1997.

[10] C.-I. Chang, *Hyperspectral Data Processing: Algorithm Design Analysis*. Hoboken, NJ, USA: Wiley, 2013.

[11] G. Chen and S.-E. Qian, "Denoising of hyperspectral imagery using principal component analysis and wavelet shrinkage," *IEEE Trans. Geosci. Remote Sens.*, vol. 49, no. 3, pp. 973–980, Mar. 2011.

[12] P. J. Curran, "Remote sensing of foliar chemistry," *Remote Sens. Environ.*, vol. 30, no. 3, pp. 271–278, 1989.

[13] D. L. Donoho and I. M. Johnstone, "Adapting to unknown smoothness via wavelet shrinkage," *J. Amer. Statist. Assoc.*, vol. 90, no. 432, pp. 1200–1224, 1995.

[14] M. Dorigo, M. Birattari, and T. Stutzle, "Ant colony optimization," *IEEE Comput. Intell. Mag.*, vol. 1, no. 4, pp. 28–39, Nov. 2006.

[15] G. Fitzgerald, D. Rodriguez, and G. O'Leary, "Measuring and predicting canopy nitrogen nutrition in wheat using a spectral index—The canopy chlorophyll content index (CCCI)," *Field Crops Res.*, vol. 116, no. 3, pp. 318–324, Apr. 2010.

[16] J. A. Gamon, L. Serrano, and J. S. Surfus, "The photochemical reflectance index: An optical indicator of photosynthetic radiation use efficiency across species, functional types, and nutrient levels," *Oecologia*, vol. 112, no. 4, pp. 492–501, 1997.

[17] C. A. Garillos-Manliguez and J. Y. Chiang, "Multimodal deep learning and visible-light and hyperspectral imaging for fruit maturity estimation," *Sensors*, vol. 21, no. 4, p. 1288, Feb. 2021.

[18] D. M. Gates, H. J. Keegan, J. C. Schleter, and V. R. Weidner, "Spectral properties of plants," *Appl. Opt.*, vol. 4, no. 1, pp. 11–20, 1965.

[19] A. A. Gitelson, Y. Gritz, and M. N. Merzlyak, "Relationships between leaf chlorophyll content and spectral reflectance and algorithms for non-destructive chlorophyll assessment in higher plant leaves," *J. Plant Physiol.*, vol. 160, no. 3, pp. 271–282, 2003.

[20] V. M. Gomes, A. M. Fernandes, A. Faia, and P. Melo-Pinto, "Comparison of different approaches for the prediction of sugar content in new vintages of whole port wine grape berries using hyperspectral imaging," *Comput. Electron. Agricult.*, vol. 140, pp. 244–254, Aug. 2017.

[21] M. K. Griffin and H. K. Burke, "Compensation of hyperspectral data for atmospheric effects," *Lincolm Lab. J.*, vol. 14, no. 1, pp. 29–54, 2003.

[22] A. Hassanzadeh, S. P. Murphy, S. J. Pethybridge, and J. van Aardt, "Growth stage classification and harvest scheduling of snap bean using hyperspectral sensing: A greenhouse study," *Remote Sens.*, vol. 12, no. 22, p. 3809, Nov. 2020.

[23] A. Hassanzadeh, J. V. Aardt, S. P. Murphy, and S. J. Pethybridge, "Yield modeling of snap bean based on hyperspectral sensing: A greenhouse study," *J. Appl. Remote Sens.*, vol. 14, no. 2, p. 024519, 2020.

[24] A. Hassanzadeh, F. Zhang, J. van Aardt, S. P. Murphy, and S. J. Pethybridge, "Broadacre crop yield estimation using imaging spectroscopy from unmanned aerial systems (UAS): A field-based case study with snap bean," *Remote Sens.*, vol. 13, no. 16, p. 3241, Aug. 2021.

[25] D. M. Hawkins, "The problem of overfitting," *J. Chem. Inf. Comput. Sci.*, vol. 44, no. 1, pp. 1–12, Jan. 2004.

[26] C. He, J. Xing, J. Li, Q. Yang, and R. Wang, "A new wavelet threshold determination method considering interscale correlation in signal denoising," *Math. Problems Eng.*, vol. 2015, Jan. 2015, Art. no. 280251.

[27] A. Huete, C. Justice, and H. Liu, "Development of vegetation and soil indices for MODIS-EOS," *Remote Sens. Environ.*, vol. 49, no. 3, pp. 224–234, Sep. 1994.

[28] M. Jansen, *Noise Reduction by Wavelet Thresholding*, vol. 161. Springer, 2012.

[29] Y. Jiang, H. Li, and M. Rangaswamy, "Deep learning denoising based line spectral estimation," *IEEE Signal Process. Lett.*, vol. 26, no. 11, pp. 1573–1577, Nov. 2019.

[30] C. F. Jordan, "Derivation of leaf-area index from quality of light on the forest floor," *Ecology*, vol. 50, no. 4, pp. 663–666, 1969.

[31] H. F. Kaiser, "The application of electronic computers to factor analysis," *Educ. Psychol. Meas.*, vol. 20, no. 1, pp. 141–151, 1960.

[32] J. P. Kerekes and J. E. Baum, "Hyperspectral imaging system modeling," *Lincoln Lab. J.*, vol. 14, no. 1, pp. 117–130, 2003.

[33] R. Khodabakhshian, B. Emadi, M. Khojastehpour, and M. R. Golzarian, "Determining quality and maturity of pomegranates using multispectral imaging," *J. Saudi Soc. Agricult. Sci.*, vol. 16, no. 4, pp. 322–331, Oct. 2017.
[34] S. Kuching, "The performance of maximum likelihood, spectral angle mapper, neural network and decision tree classifiers in hyperspectral image analysis," *J. Comput. Sci.*, vol. 3, no. 6, pp. 419–423, Jul. 2007.
[35] S. Kumar, J. Ghosh, and M. M. Crawford, "Best-bases feature extraction algorithms for classification of hyperspectral data," *IEEE Trans. Geosci. Remote Sens.*, vol. 39, no. 7, pp. 1368–1379, Jul. 2001.
[36] V. Kumar and S. Minz, "Feature selection: A literature review," *Smart Comput. Rev.*, vol. 4, no. 3, pp. 211–229, 2014.
[37] M. Lang, H. Guo, J. E. Odegard, C. S. Burrus, and R. O. Wells, "Noise reduction using an undecimated discrete wavelet transform," *IEEE Signal Process. Lett.*, vol. 3, no. 1, pp. 10–12, Jan. 1996.
[38] F. Li *et al.*, "Remotely estimating aerial n status of phenologically differing winter wheat cultivars grown in contrasting climatic and geographic zones in China and Germany," *Field Crops Res.*, vol. 138, pp. 21–32, Oct. 2012.
[39] J. Li, W. Huang, and X. Tian, "Fast detection and visualization of early decay in citrus using Vis-NIR hyperspectral imaging," *Comput. Electron. Agricult.*, vol. 127, pp. 582–592, Sep. 2016.
[40] X. Li *et al.*, "SSC and pH for sweet assessment and maturity classification of harvested cherry fruit based on NIR hyperspectral imaging technology," *Postharvest Biol. Technol.*, vol. 143, pp. 112–118, Sep. 2018.
[41] B. Lu, P. Dao, J. Liu, Y. He, and J. Shang, "Recent advances of hyperspectral imaging technology and applications in agriculture," *Remote Sens.*, vol. 12, no. 16, p. 2659, Aug. 2020.
[42] H. Ma *et al.*, "Spectral difference analysis and identification of different maturity blueberry fruit based on hyperspectral imaging using spectral index," *Int. J. Agricult. Biol. Eng.*, vol. 12, no. 3, pp. 134–140, 2019.
[43] S. Ma and J. Huang, "Penalized feature selection and classification in bioinformatics," *Briefings Bioinform.*, vol. 9, no. 5, pp. 392–403, 2008.
[44] R. Mcroberts and E. Tomppo, "Remote sensing support for national forest inventories," *Remote Sens. Environ.*, vol. 110, no. 4, pp. 412–419, Oct. 2007.
[45] S. Munera, J. M. Amigo, J. Blasco, S. Cubero, P. Talens, and N. Aleixos, "Ripeness monitoring of two cultivars of nectarine using VIS-NIR hyperspectral reflectance imaging," *J. Food Eng.*, vol. 214, pp. 29–39, Dec. 2017.
[46] J. R. Myers *et al.*, "Improving the health benefits of snap bean: Genome-wide association studies of total phenolic content," *Nutrients*, vol. 11, no. 10, p. 2509, Oct. 2019.
[47] B. M. Nicolaï, "Nondestructive measurement of fruit and vegetable quality by means of NIR spectroscopy: A review," *Postharvest Biol. Technol.*, vol. 46, no. 2, pp. 99–118, Nov. 2007.
[48] F. Pedregosa *et al.*, "Scikit-learn: Machine learning in Python," *J. Mach. Learn. Res.*, vol. 12, pp. 2825–2830, Nov. 2011.
[49] F. Piazzolla, M. L. Amodio, and G. Colelli, "Spectra evolution over on-vine holding of Italia table grapes: Prediction of maturity and discrimination for harvest times using a Vis-NIR hyperspectral device," *J. Agricult. Eng.*, vol. 48, no. 2, pp. 109–116, 2017.
[50] D. M. W. Powers, "Evaluation: From precision, recall and F-measure to ROC, informedness, markedness and correlation," 2020, *arXiv:2010.16061*.
[51] P. Rajkumar, N. Wang, G. EImasry, G. S. V. Raghavan, and Y. Gariepy, "Studies on banana fruit quality and maturity stages using hyperspectral imaging," *J. Food Eng.*, vol. 108, no. 1, pp. 194–200, Jan. 2012.
[52] B. Rasti, P. Scheunders, P. Ghamisi, G. Licciardi, and J. Chanussot, "Noise reduction in hyperspectral imagery: Overview and application," *Remote Sens.*, vol. 10, no. 3, p. 482, 2018.
[53] L. Ravikanth, D. S. Jayas, N. D. G. White, P. G. Fields, and D.-W. Sun, "Extraction of spectral information from hyperspectral data and application of hyperspectral imaging for food and agricultural products," *Food Bioprocess Technol.*, vol. 10, no. 1, pp. 1–33, Jan. 2017.
[54] M. Robnik-Šikonja and I. Kononenko, "Theoretical and empirical analysis of ReliefF and RReliefF," *Mach. Learn.*, vol. 53, nos. 1–2, pp. 23–69, Oct. 2003.
[55] F. F. Sabins, *Remote Sensing: Principles and Applications*. Long Grove, IL, USA: Waveland Press, 2007.
[56] T. R. Sinclair, R. M. Hoffer, and M. M. Schreiber, "Reflectance and internal structure of leaves from several crops during a growing season 1," *Agronomy J.*, vol. 63, no. 6, pp. 864–868, Nov. 1971.
[57] K. D. Singh, H. S. Duddu, S. Vail, I. Parkin, and S. J. Shirtliffe, "UAV-based hyperspectral imaging technique to estimate canola (Brassica napus L.) seedpods maturity," *Can. J. Remote Sens.*, vol. 47, pp. 33–47, Jan. 2021.
[58] G. M. Smith and E. J. Milton, "The use of the empirical line method to calibrate remotely sensed data to reflectance," *Int. J. Remote Sens.*, vol. 20, no. 13, pp. 2653–2662, 1999.
[59] H. Tao *et al.*, "Estimation of crop growth parameters using UAV-based hyperspectral remote sensing data," *Sensors*, vol. 20, no. 5, p. 1296, Feb. 2020.
[60] P. J. V. Laarhoven and E. H. Aarts, "Simulated annealing," in *Simulated Annealing: Theory Application*. Dordrecht, The Netherlands: IoC, 1987, pp. 7–15.
[61] G. Van Rossum and F. L Drake, *Python Tutorial*. Amsterdam, The Netherlands: Centrum voor Wiskunde en Informatica, 1995.
[62] W. F. Velicer, "The relation between factor score estimates, image scores, and principal component scores," *Educ. Psychol. Meas.*, vol. 36, no. 1, pp. 149–159, Apr. 1976.
[63] B. Venkatesh and J. Anuradha, "A review of feature selection and its methods," *Cybern. Inf. Technol.*, vol. 19, no. 1, pp. 3–26, Mar. 2019.
[64] F. Wei, Z. Yan, T. Yongchao, C. Weixing, Y. Xia, and L. Yingxue, "Monitoring leaf nitrogen accumulation in wheat with hyper-spectral remote sensing," *Acta Ecologica Sinica*, vol. 28, no. 1, pp. 23–32, Jan. 2008.
[65] M. Weiss, F. Jacob, and G. Duveiller, "Remote sensing for agricultural applications: A meta-review," *Remote Sens. Environ.*, vol. 236, Jan. 2020, Art. no. 111402.
[66] D. Whitley, "A genetic algorithm tutorial," *Statist. Comput.*, vol. 4, no. 2, pp. 65–85, Jun. 1994.
[67] J. Xiao *et al.*, "Remote sensing of the terrestrial carbon cycle: A review of advances over 50 years," *Remote Sens. Environ.*, vol. 233, Dec. 2019, Art. no. 111383.
[68] H. R. Xu, Y. B. Ying, X. P. Fu, and S. P. Zhu, "Near-infrared spectroscopy in detecting leaf miner damage on tomato leaf," *Biosyst. Eng.*, vol. 96, no. 4, pp. 447–454, Apr. 2007.
[69] C. Yang, W. S. Lee, and P. Gader, "Hyperspectral band selection for detecting different blueberry fruit maturity stages," *Comput. Electron. Agricult.*, vol. 109, pp. 23–31, Nov. 2014.
[70] Q. Yuan, L. Zhang, and H. Shen, "Hyperspectral image denoising employing a spectral–spatial adaptive total variation model," *IEEE Trans. Geosci. Remote Sens.*, vol. 50, no. 10, pp. 3660–3677, Oct. 2012.
[71] R. Yuhas, A. F. H. Goetz, and J. W. Boardman, "Discrimination among semi-arid landscape endmembers using the spectral angle mapper (SAM) algorithm," in *Proc. 3rd Annu. JPL Airborne Geosci. Workshop*, vol. 1, Jun. 1992, pp. 147–149.
[72] C. Zhang, L. Zhou, Y. Zhao, S. Zhu, F. Liu, and Y. He, "Noise reduction in the spectral domain of hyperspectral images using denoising autoencoder methods," *Chemometric Intell. Lab. Syst.*, vol. 203, Aug. 2020, Art. no. 104063.
[73] F. Zhang, A. Hassanzadeh, J. Kikkert, S. J. Pethybridge, and J. van Aardt, "Comparison of UAS-based Structure-from-Motion and LiDAR for structural characterization of short broadacre crops," *Remote Sens.*, vol. 13, no. 19, p. 3975, Oct. 2021.
[74] X. Zhang and P. Li, "Lithological mapping from hyperspectral data by improved use of spectral angle mapper," *Int. J. Appl. Earth Observ. Geoinf.*, vol. 31, pp. 95–109, Sep. 2014.
[75] S. Zou, Y.-C. Tseng, A. Zare, D. L. Rowland, B. L. Tillman, and S.-C. Yoon, "Peanut maturity classification using hyperspectral imagery," *Biosyst. Eng.*, vol. 188, pp. 165–177, Dec. 2019.

Amirhossein Hassanzadeh (Student Member, IEEE) received the B.S. degree in chemical engineering from the University of Guilan, Rasht, Iran, in 2016, and the Ph.D. degree in the Imaging Science Program in 2017.

He joined the Rochester Institute of Technology (RIT), Rochester, NY, USA. He joined the Digital Imaging and Remote Sensing (DIRS) Group, RIT, in September 2018, and started working under the supervision of Jan van Aardt. He currently works on yield modeling and harvest scheduling of snap bean, as a proxy crop using unmanned aerial system (UAS) and remote sensing approaches. He is also keen on briding remote sensing to deep learning. His research is one that focuses on transitioning academia to industry by delivering packages to farmers and growers, so they can rent a drone, set up the flight lines, sit and relax while watching the drone fly on its own, uploading the data to the software, have a cup of coffee, and take actions based on the given probability map. His research interests are precision agriculture, remote sensing, hyperspectral data, and machine learning and deep learning methods.

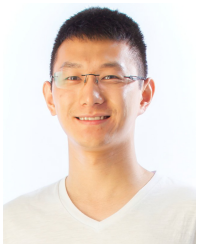

Fei Zhang (Student Member, IEEE) received the B.S. degree in optical information science and technology from Wuhan University, Wuhan, China, in 2015, and the M.S. degree in optical engineering from Zhejiang University, Hangzhou, China, in 2018. He is currently pursuing the Ph.D. degree with the Digital Imaging and Remote Sensing Laboratory, Rochester Institute of Technology, Rochester, NY, USA.

His research interests involve precision agriculture applications based on light detection and ranging (LiDAR) point clouds and multispectral images collected by unmanned aerial systems.

Sean P. Murphy (Member, IEEE) received the Associate degree in applied science with a focus on ornamental horticulture from the Finger Lakes Community College, Canandaigua, NY, USA, in 2014, and the B.T. degree in horticulture business management from the Morrisville State College, Morrisville, NY, USA, in 2016.

He joined the Horticulture Department, Cornell University, Geneva, NY, USA, in 2011, where he has been working on peas, beans, and sweet corn before moving to plant pathology in 2017 under the direction of Dr. Sarah Pethybridge. He is currently a Technician III in plant pathology with the Cornell AgriTech at The New York State Agricultural Experiment Station, Cornell University, and focuses on fungal pathogens causing diseases of broad-acre vegetable crops including table beets, snap beans, dry beans, and allium crops.

Sarah J. Pethybridge (Member, IEEE) received the B.Agr.Sc. (Hons.) and Ph.D. degrees in plant pathology from the University of Tasmania, Hobart, TAS, Australia, in 1995 and 2000, respectively.

She was an Extension Plant Pathologist with the University of Tasmania for nearly ten years, the Agricultural Research and Development Manager of the Australian pyrethrum industry, Botanical Resources Australia Pty. Ltd., Ulverstone, TAS, Australia, for three years, and the Science Group Leader (Field Crops) of the New Zealand Institute for Plant and Food Research, Auckland, New Zealand, for two years. She joined Cornell University, Ithaca, NY, USA, as an Assistant Professor of plant pathology, in 2014, where she was promoted to an Associate Professor and a Program Leader in plant pathology in 2019. At Cornell University, she works in the research and extension of a broad range of vegetable crops, including snap bean, table beet, and onion. Her research interests include quantitative epidemiology, population biology, and disease management.

Dr. Pethybridge is also an Active Member of the American Phytopathological Society and a Senior Editor for the journal, *Plant Disease*. In 2015, she received the President's Council for Cornell Women Affinito-Stewart Award, and the Cornell University College of Agriculture and Life Sciences Research and Extension Award for Early Achievement in 2018.

Jan van Aardt (Member, IEEE) received the B.S. Forestry degree in how to grow and cut down trees from Stellenbosch University, Stellenbosch, South Africa, in 1996, and the M.S. and Ph.D. Forestry degrees with a focus on remote sensing (imaging spectroscopy and light detection and ranging) from the Virginia Polytechnic Institute and State University, Blacksburg, VA, USA, in 2000 and 2004, respectively.

This was followed by post-doctoral work at the Katholieke Universiteit Leuven, Leuven, Belgium, and a stint as a Research Group Leader at the Council for Scientific and Industrial Research, Pretoria, South Africa. Imaging spectroscopy and structural [light detection and ranging (LiDAR)] sensing of natural resources form the core of his efforts, which vary between vegetation structural and system state (physiology) assessment. Stated differently, the interaction of photons with leaves is what really excites him. He is currently a Professor with the Chester F. Carlson Center for Imaging Science, Rochester Institute of Technology, Rochester, NY, USA. He has received funding from National Science Foundation (NSF), National Aeronautics and Space Administration (NASA), Google, and United States Department of Agriculture (USDA), among others. He has published more than 80 peer-reviewed papers and more than 80 conference contributions.